BSAC-1259954814

LBNL-2859E

Development of a Low-Cost Particulate Matter Monitor

Richard M. White and Justin Black
Berkeley Sensor and Actuator Center
University of California, Berkeley, CA

Michael G. Apte and Lara A. Gundel,
Environmental Energy Technologies Division
Lawrence Berkeley National Laboratory, Berkeley, CA

This work was supported by the California Air Resources Board (CARB), the Innovative Clean Air Technologies Program (ICAT), and the California Energy Commission (CEC) through Contract 02-5; by the California Tobacco-Related Disease Research Program for cost-share contributions through Grant 11RT-0202; and by the University of California, Berkeley, for in-kind funding through the academic salary of Prof. White. The study was also supported by the Assistant Secretary for Energy Efficiency and Renewable Energy, Building Technology Program of the U.S. Department of Energy under contract DE-AC02-05CH11231.

Development of a Low-Cost Particulate Matter Monitor

August 2008

Prof. Richard M. White, University of California, Berkeley, CA
Dr. Michael G. Apte and Dr. Lara A. Gundel, Co-Principal Investigators
Lawrence Berkeley National Laboratory, Berkeley, CA

Contract Number: 02-5

Amount of Contract: $291,000

Acknowledgements

The authors gratefully acknowledge the contributions made by these people:

Dr. Rossana Cambie, Post Doctoral Fellow, Engineering Division, LBNL, for mechanical modeling of the particulate monitor; and Zhuo Huang, Michael Spears, George Stern, and Elizabeth Stewart, Environmental Energy Technologies Division, LBNL, Undergraduate Laboratory Interns, for assistance with validation and field testing.

We also thank the following organizations:

The California Air Resources Board (CARB), the Innovative Clean Air Technologies Program (ICAT), and the California Energy Commission (CEC) for the support through Contract 02-5; LBNL Engineering Division for contributions to the engineering work on the monitor; the Laboratory-Directed Research and Development Program of the U.S. Department of Energy (DOE) for support of work at LBNL that led to 'proof of concept' for the PM monitor; the U.S. DOE Undergraduate Laboratory Internship Program for student support; the California Tobacco-Related Disease Research Program for cost-share contributions through Grant 11RT-0202; and the University of California, Berkeley, for in-kind funding through the academic salary of Prof. White. The study was also supported by the Assistant Secretary for Energy Efficiency and Renewable Energy, Building Technology Program of the U.S. Department of Energy under contract DE-AC02-05CH11231.

Table of Contents

Executive Summary

The purpose of this project is to develop an inexpensive device that monitors concentrations of airborne particulate matter (PM). The goal is a particulate monitor that is small, lightweight, portable and quite sensitive. PM is a major public health issue, and there is an urgent need for inexpensive devices that monitor PM in epidemiological studies of aerosol exposure effects and exposure to pollutants such as diesel exhaust, environmental tobacco smoke, and power plant emissions. Such tools could also be applied to ventilation control for better indoor air quality with lower energy expenditure, monitoring airplane cabin air quality and improving industrial hygiene. The PM monitor described in this report could thus be of substantial value to the State of California.

This project is based on initial work at LBNL to monitor airborne particulate matter concentrations by using thermophoresis – motion of particles induced by a thermal gradient – to deposit particles on a piezoelectric resonator whose resonant frequency falls in proportion to the mass deposited. The present project uses microfabricated elements as the thermophoretic source and the mass-sensing resonator. (The acronym MEMS – for micro-electro-mechanical system, applies to this type of system.) The project is the result of collaboration between researchers at LBNL and the Berkeley Sensor and Actuator Center (BSAC) on the Berkeley campus of the University of California. The MEMS PM monitor currently has a limit of detection of 18 $\mu g\ m^{-3}$ for 24 hour sampling. Several large instrument manufacturers have expressed commercial interest in this device, as well as in use of its mass-sensing module in other instruments.

During this study, the optical component of the device was not fully implemented and has been left for future efforts. Suggested improvements in the current prototype include use of integrated thermal correction, reconfiguration of the resonator for increased particle collection area, increased thermophoretic collection efficiency using an increased temperature gradient, and shielding the resonator electronics from deposition of ultrafine particles.

Abstract

We describe a small, inexpensive portable monitor for airborne particulates, composed of the following elements:

a. A simple size-selective inlet (vertical elutriator) that permits only particles below a pre-set diameter to pass and enter the measurement section;
b. A measurement section in which passing particles are deposited thermophoretically on a micro-fabricated resonant piezoelectric mass sensor;
c. An optical characterization module co-located with the mass sensor module that directs infrared and ultraviolet beams through the deposit. The emergent optical beams are detected by a photodiode. The optical absorption of the deposit can be measured in order to characterize the deposit, and determine how much is due to diesel exhaust and/or environmental tobacco smoke; and
d. A small pump that moves air through the device, which may also be operated in a passive mode.

The component modules were designed by the project team, and fabricated at UCB and LBNL. Testing and validation were performed in a room-sized environmental chamber at LBNL in to which was added either environmental tobacco smoke (ETS, produced by a cigarette smoking machine) or diesel exhaust (from a conventional diesel engine). Two pilot field tests in a dwelling compared the monitor with existing aerosol instruments during exposure to infiltrated ambient air to which cigarette smoke, diesel exhaust, wood smoke and cooking fumes were added. The limit of detection (LOD) derived from statistical analysis of field data is 18 $\mu g\ m^{-3}$, at the 99% confidence level. The monitor weighs less than 120 g and has a volume of roughly 250 cm^3. Power consumption is approximately 100 milliwatts.

During this study, the optical component of the device was not fully implemented and has been left for future efforts. Suggested improvements in the current prototype include use of integrated thermal correction, reconfiguration of the resonator for increased particle collection area, increased thermophoretic collection efficiency using an increased temperature gradient, and shielding the resonator electronics from deposition of ultrafine particles.

1. Introduction

1.a. Background

The purpose of this project is to develop an inexpensive device that monitors concentrations of airborne particulate matter (PM). The goal is a particulate monitor that is small, lightweight, portable and quite sensitive. PM is a major public health issue, causing about 65,000 excess U.S. deaths per year and large associated morbidity (Refs. 1, 2). Since exposures are not well known and currently no affordable population-based exposure assessment tools exist, there is an urgent need for inexpensive devices that monitor PM. Such monitors could be used in epidemiological studies of aerosol exposure effects and exposure to pollutants such as diesel exhaust, environmental tobacco smoke, and power plant emissions. Such tools could also be applied to ventilation control for better indoor air quality with lower energy expenditure, monitoring airplane cabin air quality and improving industrial hygiene. Compact particle *mass* sensors could also expand the capabilities of current aerosol instruments that are limited to measuring particle *number* concentrations. The PM monitor described in this report could thus be of substantial value to the State of California.

In the 1970's TSI, Inc. developed real-time PM mass monitoring instruments for industrial hygiene applications. References 3-6 describe the main features of these piezobalances (based on the piezoelectric effect) and summarize results for monitoring a variety of aerosols. Electrostatic precipitation directed airborne particles towards a quartz crystal whose resonant frequency decreased as the PM mass increased. To observations from these studies point to issues that could influence the performance of MEMS PM monitors: 1) the influence of relative humidity (RH), since collection efficiency decreased when RH dropped below 30%; and 2) the source or nature of the particles, since the range of linear response per unit added mass showed some dependence on the type of particles.

1.b. Overview

This project is based on initial work at LBNL to monitor airborne particulate matter concentrations by using thermophoresis – motion of particles induced by a thermal gradient – to deposit particles on a piezoelectric resonator whose resonant frequency falls in proportion to the mass deposited. The present project uses microfabricated elements as the thermophoretic source and the mass-sensing resonator. (The acronym MEMS – for micro-electro-mechanical system, is applicable to this type of system. The new monitor was called the MEMS-PEA, for "MEMS personal exposure assessment" monitor, in the proposal submitted to ICAT in 2002. This report refers to the new device as the "MEMS PM monitor" because its applications are not limited to personal exposure assessment.) The project is the result of collaboration between researchers at LBNL and the Berkeley Sensor & Actuator Center on the Berkeley campus of the University of California. A list of the project personnel appears in Appendix 1.

1.c. Objectives

We sought technology that would result in a particulate monitoring system that would be

i. Capable of measuring concentrations at typical ambient levels (e.g., μg m^{-3}) in near real-time, while providing information on particulate composition, and
ii. Compact, lightweight, battery powered, inexpensive, quiet, and able to match 24-hr PM concentrations found using Federal Reference Methods for monitoring concentrations of airborne particulate matter in two size ranges: below 2.5 and 10 μm diameter ($PM_{2.5}$ and PM_{10}, respectively).

In addition, it would be desirable to have a monitor that could be integrated with modern communication devices such as cell phones or iPods™.

2. Approach

The project involved design, fabrication and testing of the main components of the MEMS PM monitor, in coordination with engineering design and fabrication of the packaging that integrated the components into a functioning prototype. Performance evaluation took place in a room-sized environmental chamber at LBNL using mainly well-characterized environmental tobacco smoke (ETS) in ambient air as the challenge aerosol, followed by limited testing with diesel exhaust. As part of a pilot field study, the prototype MEMS PM monitor operated in a residence in Berkeley. Periodically the nearby ambient PM was enriched with low levels of PM from sources such as ETS, diesel exhaust, cooking or wood smoke. The data from the MEMS PM monitor were compared to data from other aerosol instruments in both environmental chamber testing and pilot field study.

2.a. Organization of the MEMS PM monitor

Figure 1 shows the arrangement of the main components of the MEMS PM monitor. The inlet faces downward so that PM size-selection is based on the difference between size-dependent gravimetric settling and the upward movement of air by a small pump or fan at the top. As shown in more detail in Sec. 2.b. where the mechanical design is shown, the rectangular sections between the inlet and outlet form a continuous open channel through which PM-laden air passes. The collector could also be designed to use only the natural buoyancy of air. The central section of the channel has reduced height in the region where the particles are deposited by thermophoresis, weighed by piezoelectric resonators and optically examined by light-emitting diodes and photodiodes.

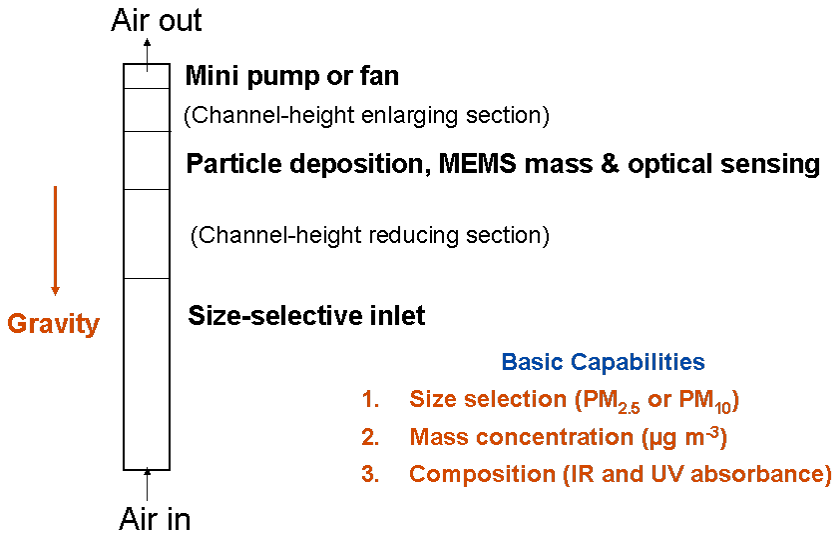

Figure 1. Schematic diagram of the components of the particulate monitor. The sections of the device (rectangles in the Figure) through which air flows from bottom to top are identified at the right.

2.b. Mechanical design

Views of the monitor appear in Figs. 2 and 3. In actual use, the monitor is oriented so that its air flow is upward against the force of gravity. For convenience, the views shown in Fig 2 have been rotated 90° counter-clockwise from the vertical orientation used for PM sampling. The 500-μm-high channel for air flow is formed by metal parts on top and bottom, and by metal side walls that establish the channel width (2.9 mm). One of the plurality of mass-sensing film bulk acoustic resonators (FBARs, described in Sec. 2c), is shown below the channel. The FBARs are mounted on a printed-circuit board (PCB) to which the remaining components are fastened. The quartz-supported resistive heaters that cause thermophoretic deposition are mounted at the top of the channel, directly above the FBARs. In this design, the optical beams from the IR (infrared) and UV (ultraviolet) light-emitting diodes pass through the semi-transparent heater, reflect from the deposit-coated resonator and ultimately are detected by the photodiode array shown at the top of the assembly above. An improved design for optical characterization (not shown here) has the LEDs near the FBARs and under the TP heaters. This allows for PM deposition directly above the LEDs the for light transmission measurements.

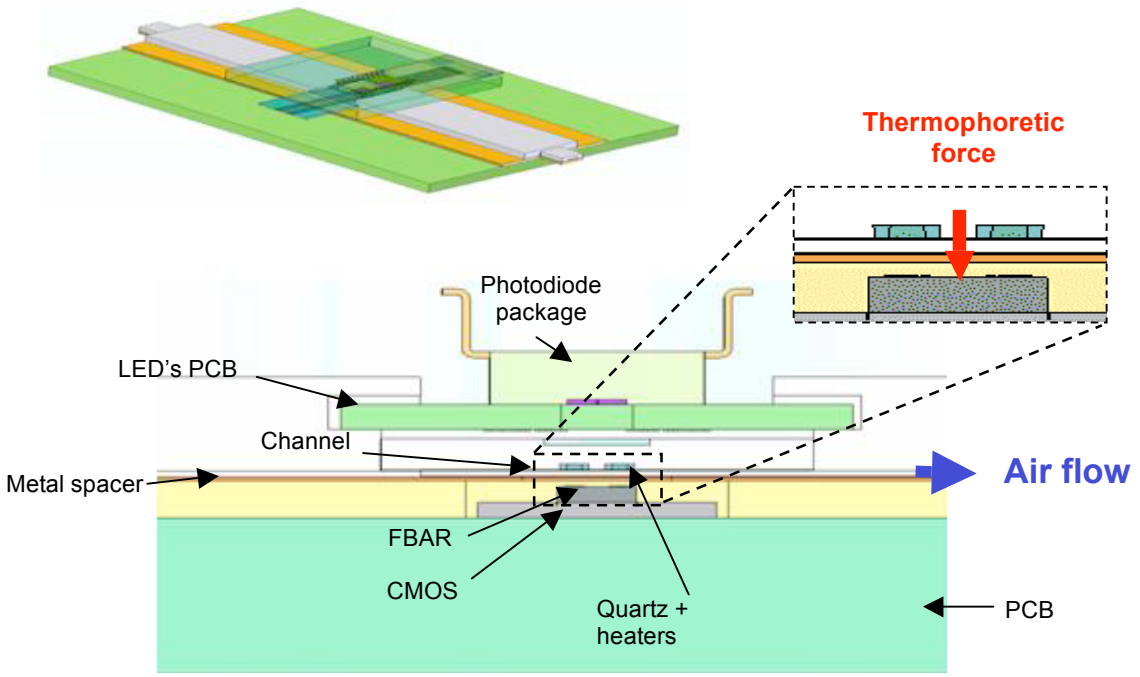

Figure 2. Section views of the central section of the PM monitor. The upper left shows the central section of the PM monitor, in a view created with SoldWorks® software. The lower part of the Figure shows a cross-section view of the particle collection and monitoring region, which is the core of the actual device shown below in Fig. 3.

Photos of the MEMS PM monitor that was used for laboratory and field validation studies are shown in Figure 3, in a tabletop view. In the lower view the PCBs have been removed to show the central PM collecting region.

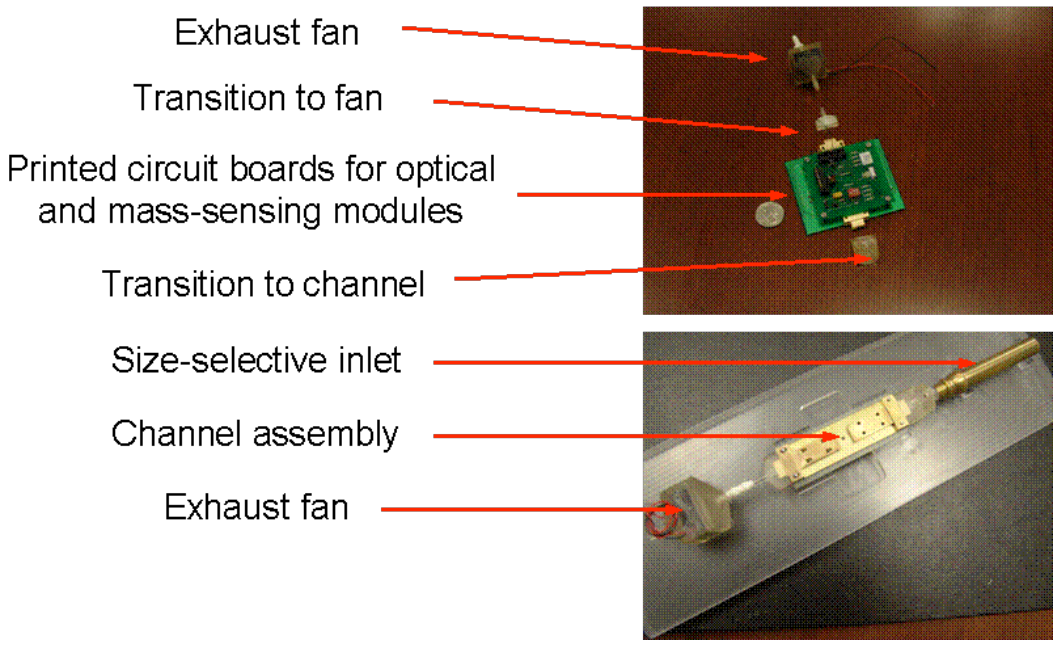

Figure 3. Photos of prototype MEMS PM monitor components in the configuration used for laboratory and field validation. *Upper photo:* from bottom to top, direction of air flow: the plastic transition from the size-selective inlet (not shown) to the 0.5-mm-high rectangular channel, the measurement modules, with the channel assembly between the printed circuit boards, the plastic transition from the channel to the fan used to draw air through the monitor. A U.S. quarter is shown at the left for scale. *Lower photo:* The printed circuit boards have been removed to show the particle collection region. Air flow is right to left. The fan is at the lower left, and the size-selective inlet is at the upper right. In actual use, the axis of the monitor is vertical, with the size-selective inlet (SSI) pointing downward.

2.c. Components: design and performance

Each major component of the MEMS PM monitor is described below, in order of air flow through the channel. Design, materials and general performance characteristics are addressed in this Section. Section 3 presents data acquired using the assembled monitor during exposure to controlled concentrations of ETS and diesel exhaust in a room-sized environmental chamber at LBNL. Section 3b presents data acquired with the assembled monitor in a Berkeley residence where infiltrating ambient air was periodically enriched with common PM sources.

2.c.i. Size-selective inlet and air mover

The downward facing size selective inlet (SSI) used in the current MEMS PM monitor uses the concept of vertical elutriation (Ref. 7). At the cut-point diameter, the

gravitational force is balanced by the upward viscous drag force caused by pulling air through the vertical channel at a constant rate. Smaller diameter particles are accelerated into the sampler, while those with terminal settling velocities greater than the sample velocity are rejected. The particle cut-point is determined by the diameter of the opening of the SSI, the flow rate of air into the inlet, and particle density. Terminal settling velocity of atmospheric aerosol particles is linearly proportional to particle density which can range from about 1.2 to 2.0 g cm^{-3}, with a typical density of about 1.6 g cm^{-3} (Ref. 8). The cut point shifts about 0.1 micron per 10% change in particle density. Figure 4 shows the results of an experiment with a scaled model of an SSI that was designed to exclude particles larger than about 1 µm (challenge aerosol was ambient air with a low concentration of talc suspended in it to increase the coarse fraction), whereas the SSI for MEMS monitor has been designed to collect $PM_{2.5}$. (The purpose of this early experiment was to establish proof of concept for the SSI design, not to create a $PM_{2.5}$ inlet.) Particles of 1.1 µm diameter were predicted to experience equal upward and downward forces. Experimental results showed that roughly 35% of the PM of this diameter passed through the SSI. The observed 50% cut-point was about 0.6 µm. To collect $PM_{2.5}$ the SSI for MEMS monitor has an inner diameter of 1.0 cm and sample stream velocity of 0.02 cm/sec (sampling rate = 1 standard cm^3 min^{-1}).

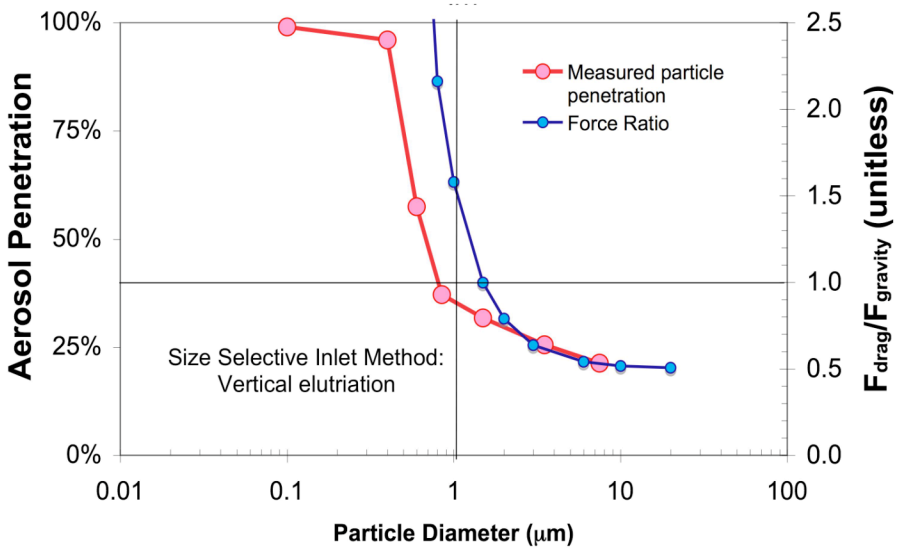

Figure 4. Results of an experiment showing how transmission through a size-selective inlet cuts off for particles with diameters larger than a given value.

Separation by size in the SSI occurs because the downward gravitational force on the larger particles exceeds the upward viscous drag force on them. The data in Figure 4 were acquired with a laser optical particle counter having a 31 cm diameter inlet and sampling at 2.8 L min^{-1}. The SSI for the prototype MEMS PM monitor is designed to exclude particles less than 2.5 µm in diameter.

As discussed above, gravitational settling rates of particles depend on particle density. Additionally, structure and composition (especially for very small carbonaceous chain aggregates) can affect the apparent settling rates and thus add to the uncertainty of total mass measurement. Fortunately, in many cases these very small particles make up a miniscule portion of total PM mass due to their small volume. More effort is needed to characterize thoroughly the gross behavior and size separation of aerosol samples as they are affected by the shape and dimensions of this SSI design.

Since the SSI operation is dependent on having a vertical inlet with respect to gravity, significant deviation from this orientation will affect the inlet cut size. In the worst case, where the inlet is completely inverted, no particle size rejection will occur. This may limit this SSI design options for use with personal samplers, but for a free-standing device should pose no real problem. A free-hanging inlet or inlet-sampler combination could be gimbaled to remain plumb.

The SSI requires constant air flow to maintain a steady cut-point diameter and for determination of mass concentration. Because neither the SSI nor collection of PM by thermophoresis offers much resistance to air flow, a low-power fan or pump can drive air flow, and a critical orifice can be used to control the flow rate. Furthermore, this type of inlet will not clog like an impactor nozzle. Prototype MEMS PM monitors first used a 25 mm square laptop computer fan (Sunon Fan, Model KDE0502PFB1-8V), and later a 15 mm diameter rotary vane pump (Schwarzer Precision Pumps, Model 135 FZ). Because of its smaller physical size and lower power consumption (0.12W for the 25 mm square fan vs. 0.02W for the 15 mm diameter pump), the pump is the better choice. The prototype MEMS PM monitor was operated at a flow rate of 1.5 cm^3 min^{-1} during the chamber and field testing. The monitor may also be operated in a passive mode, where a natural temperature gradient causes air to flow through the device.

2.c.ii. Thermophoretic deposition module

The principle of thermophoretic deposition and some related experimental results are shown in Figure 5. In Fig. 5a, PM-laden air flows from left to right through a section whose upper and lower wall temperatures are 22 ^oC and 100 ^oC, respectively. Each particle experiences a thermophoretic force that is proportional to the temperature gradient, ∇T. This force drives the particles toward the cool surface, where they impact on the upper wall and adhere as a result of the van der Waals force. Fig. 5b, from Ref. 9 has experimental and modeling data that show that particle collection efficiency increases as the thermal gradient increases. These results suggest that collection approaches 100% in the MEMS PM monitor because of the larger temperature gradient ($\nabla T \sim 1600$ K cm^{-1}).

Figure 5. Principle and characteristics of thermophoretic deposition.

(5a)

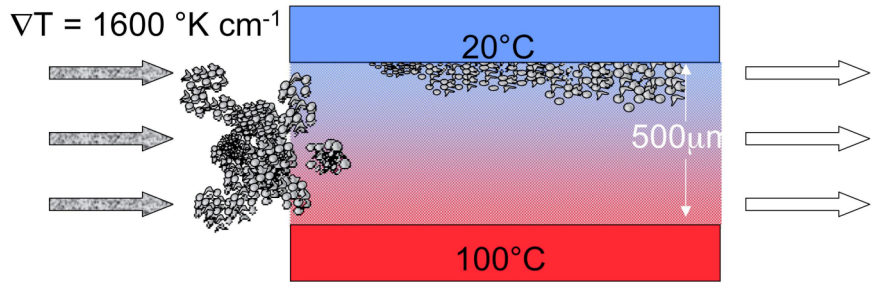

- Thermophoretic (TP) force ~ ∇T
- Adherence: Van der Waals forces
- TP collection very efficient for sub-micron and nanoparticles

Fig. 5a (above) The drawing shows how particles deposit on the cooler surface as they pass through a section whose upper and lower walls are at 22°C and 100°C, respectively.

(5b)

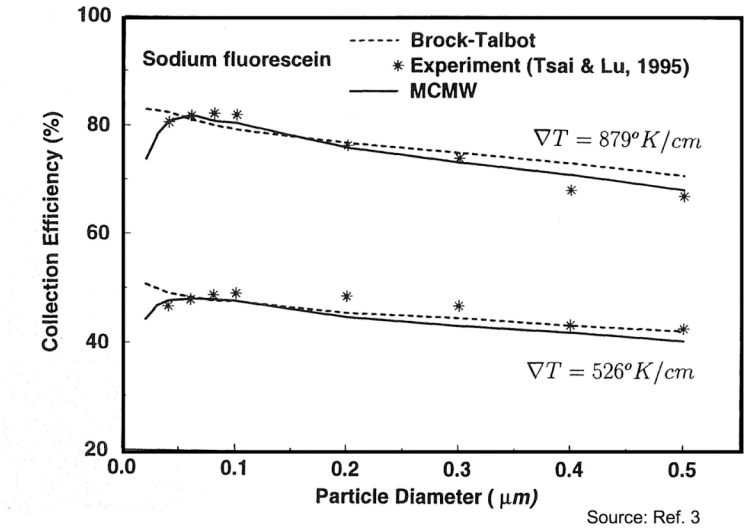

Figure 5b. Plots of experimental and theoretical studies showing that collection efficiency increases with the thermal gradient (see Ref. 9 for identification of sources in the legend at upper right of this Figure).

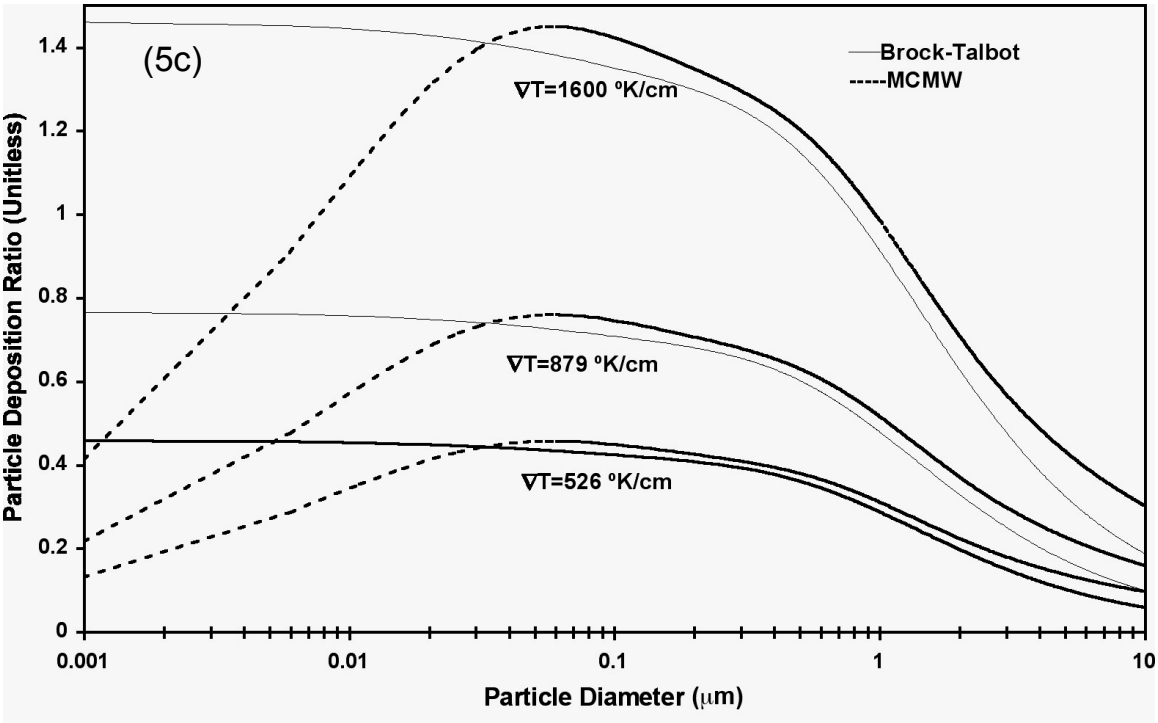

Figure 5c. The Brock-Talbot and MCMW models used by He and Ahmadi (Ref. 9) predicting the particle deposition ratio (collection efficiency) for the 1600 °K cm^{-1} thermal gradient used in the MEMS PM monitor compared to the lower ratios shown in Figure 5b.

According to He and Ahmadi (Ref. 9), the thermophoretic collection efficiency is

$$\eta = U_{th} L/2hu_m$$

where U_{th} is the thermophoretic velocity, u_m is the mean air velocity, and L and h are the length and the height of the channel. In Figure 5c, the y-axis shows the ratio of immediate thermal velocity toward the cold surface to the axial velocity, after taking into account the dimensions of the channel. Both the Brock-Talbot and MCMW models are plotted with the parameters presented by He and Ahmadi. In Figure 5c, the two curves are the predictions of the models for each gradient. This assumes that the dimensions of the channel are the same as in the simulation by He and Ahmadi. The molecular diameter of air is chosen to be 5.7 nm, and the aerosol particles consist of NaCl having thermal conductivity k = 6.69 W m^{-1} K^{-1}. The models predict much better collection efficiency for PM with this thermal gradient than with the weaker gradients used by He and Ahmadi. Figure 5c also expands the deposition model results from 1nm to 10 μm, and it shows that deposition drops off above a few microns but is still relatively effective below 2.5 microns. The MCMW model shows a strong dropoff below about 10 μm, but this particle size has little relevance to environmental PM mass measurement.

The MEMS PM monitor uses semi-transparent heaters through which the interrogating optical beams can pass. Fig. 6 shows images of the resistive thin-film heaters formed on a thin quartz sheet, along with their temperature-power characteristics.

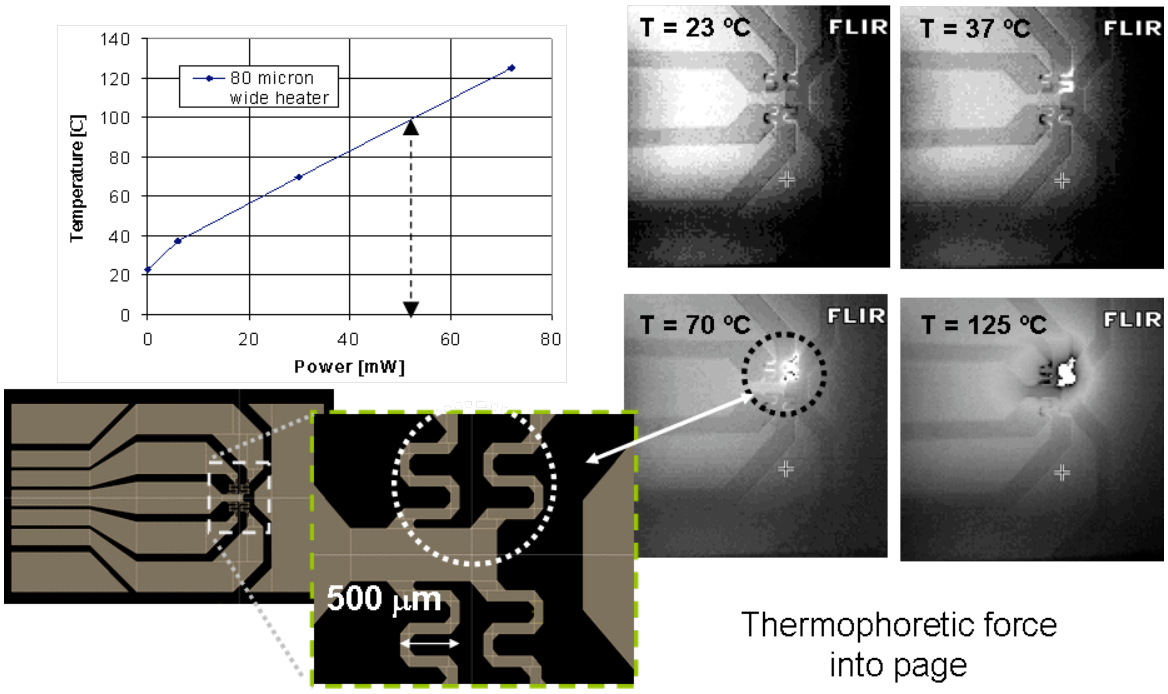

Figure 6. **Microfabricated thermophoretic heaters and their characteristics. *Lower left:* Visible light microscope images of four resistive heaters on a transparent quartz support. *Upper right:* Forward-looking infrared (FLIR) images taken as a single heater (circled) is energized. False color indicates temperature; brighter regions are at higher temperatures. *Upper left:* Heater temperature (°C) vs. electrical power required (milliwatts) for a single heater element.**

The heaters were fabricated at UCB by patterning thin deposits of polycrystalline silicon onto thin quartz sheets. In separate experiments, light transmission through a 1 μm thick polysilicon film on a 500 μm thick quartz substrate was found to be 55% and 2% at 810 nm and 370 nm, respectively.

The lower left corner of Fig. 6 shows images of four serpentine heater elements (the lighter curvy areas of the inset diagram) acquired from a CAD layout of the heater. Each turn of a heater is about 500 microns across, and the resistive elements are 80 microns wide. (For scale, the diameter of a human hair ranges from 70 to 100 microns.) The upper right section of Fig. 6 shows patterns of heating produced with four different amounts power, as shown in the plot at upper left. The photos were acquired using forward-looking infrared (FLIR) instrumentation. Particulate deposition occurs for heater temperatures of about 100°C, using only about 50 milliwatts of power, as shown in the upper left section of Fig. 6.

To verify that the micro-fabricated thermophoretic heaters would actually cause particulate deposition at heater temperatures of about 100°C, the heater assembly was

oriented 500 μm from an evaporated Al film on a silicon chip and packaged in the MEMS-PM housing. ETS was sampled at 20 cm^3 min^{-1} using a peristaltic pump.

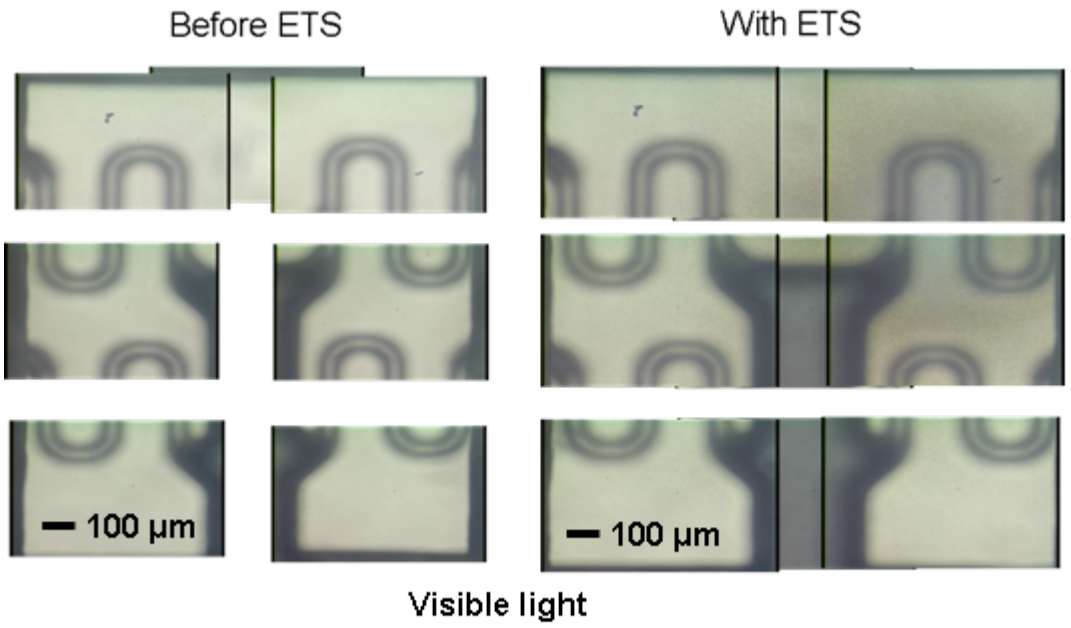

Figure 7. Composite optical images of the polished aluminum surface as seen through the thermophoretic heaters, taken in visible light with a Reichert-Jung Polylite microscope. On the left: Before exposure to ETS. On the right: after exposure to ETS , with the upper right heater energized.

Figure 7 shows images of the aluminum surface taken through the heater, in visible light, before (left) and after (right) exposure to ETS while the heater at the upper right was energized. Each side of the figure is composed of a set of images taken with a microscope in which the chip size was larger than the microscope field of view. Thus, in order to obtain a high resolution image, the photo was segmented into a 5 x 5 array, each taken with a 5x objective illuminated with visible light. The black lines depict the boundaries of each photo.

The composite image on the right has a brown halo surrounding the inverted U (central section) of the heater in the top right corner. Through the eyepiece of the microscope the experimenter saw the most ETS deposition in the central area between the arms of the inverted U, whereas the camera rendered this area as lighter. When the deposit was viewed in UV light a similar pattern of deposition was observed. Thus, we verified that the microfabricated thermophoretic deposition component of the MEMS PM device is indeed working properly.

2.c.iii. Mass-sensing module

It is well known that an acoustic resonator can be used to measure the mass of a deposited thin film – the added mass reduces the resonant frequency, which can be measured quite precisely (Ref. 10). This principle is used in commercial vacuum deposition systems and has long been used by chemists to weigh electrodeposited films.

The initial LBNL work mentioned above used a one-cm-diameter piezoelectric resonator crystal assembly known as a quartz crystal microbalance (QCM) operating at 10 MHz. For the MEMS-based monitor, we use a microfabricated film bulk acoustic resonator (FBAR) whose transverse dimensions are only 150 by 150 square microns and whose resonant frequency is approximately 1.6 GHz, roughly 270 times higher than that of the QCM. In addition to its smaller size, which is quite attractive, the theoretical mass detection limit of the FBAR is approximately 70 times lower than that of the QCM (see Fig. 8). Because of the small size -- the FBAR area is roughly 10 thousand times smaller than that of the QCM assembly – a number of FBAR resonators can be used in the instrument, and the resonator array can be built atop an electronic circuit chip that can be used to select which resonator is active for a given measurement. This type of circuit chip is known as a CMOS circuit and is in common use. The FBAR itself is also in wide use today for electronic filtering applications in cell phones (see Ref. 11). Thus we are building on two familiar technologies in wide use today. For our application, the ability to select one from a number of similar resonators extends the operating lifetime, since, as a particular resonator becomes saturated, one simply switches to a fresh resonator.

QCM

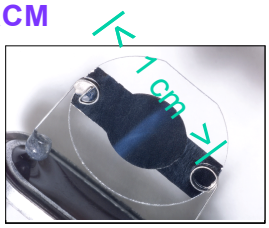

FBAR

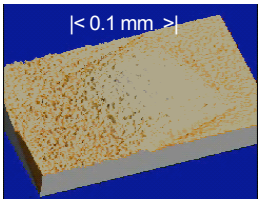

Sensor	Device Description	Typical Operating Frequency (MHz)	Calculated Theoretical Mass Detection Limit (ng/μm²)
Quartz Crystal Microbalance (QCM)	AT-cut Quartz	6	0.70
Surface Acoustic Wave (SAW)	ST-cut Quartz	100 -500	0.08
Flexural Plate Wave (FPW)	Micro -fabricated ZnO, SiN,Al	2 - 5	0.02
Film Bulk Acoustic Resonators (FBAR)	Micro -fabricated ZnO, SiN,Al,Au	1000 - 2000	0.01

- FBAR: sensitive to ~ 1pg
- FBAR: capacity ≥ 1 ng
- Easy to micro -fabricate
- FBAR: arrays 2x2 to 10x10
- PM mass sensor on a chip

Figure 8. Comparison of various mass-sensing acoustic-wave resonators. Images of the QCM and the FBAR sensors appear at the left.

We fabricated FBARs at UC Berkeley and also studied commercially made FBARs (from Agilent, Inc.). Zinc oxide (ZnO) and aluminum nitride (AlN) devices were studied. In one test, an aluminum thin film of known thickness, and hence mass, was deposited on an FBAR and the reduction of the FBAR frequency was measured; this test indicated that an added mass per unit area as small as 10 picograms per square micron could be detected. (The detection limit is defined here as the level where the signal falls to just three times the noise level.)

Figure 9 shows the fabrication process flow for making one of these FBARs. The left side of Fig. 9 is a top view; the black square in the center shows the active area of the resonator. The cross-section view on the right shows how the FBAR is mounted in the channel of the monitor; the sampled air passes across the chip to the right, particles are deposited thermophoretically because of the presence of the heater above the FBAR. This FBAR is fabricated on top of a thin film of silicon nitride that was in turn formed on top of a silicon wafer; the etched bathtub-shaped region beneath the FBAR permits the resonator to vibrate freely while its oscillation frequency is being measured during deposition. With the FBAR and polysilicon heater configured as in the MEMS PM monitor (heater positioned 500 µm above the FBAR), a heater temperature of 100 ºC induced only about a 1.5 ºC increase in FBAR temperature. This small temperature increase at the FBAR surface should prevent condensation of water during ambient sampling, but it is probably not sufficient to cause significant volatilization losses of other semi-volatile species. The high thermal conductivity of the AlN film and proximity of the FBAR to the underlying silicon substrate provided heat dissipation paths with low thermal resistance.

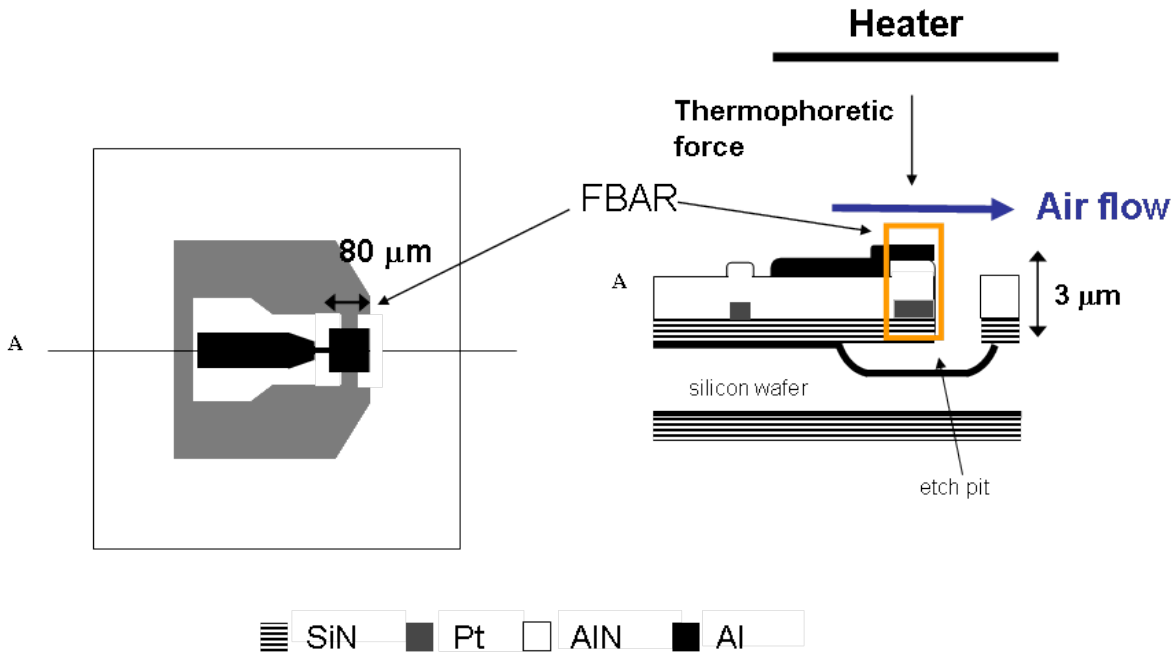

Figure 9. Process flow for making FBAR mass sensors. See text for details.

In the assembled monitor, each heater section concentrates PM deposition over an area (~500 μm X 600 μm) that is larger by a factor of 13 than the mass sensing region of the FBAR, which has dimensions of ~150 μm X 150 μm. Measurement of the PM collection efficiency and mass sensitivity of the monitor must account for the fact that PM deposits on and around the mass-sensing component of the MEMS PM monitor in its current configuration.

The temperature dependence of the FBAR mass sensor in the MEMS PM monitor is due to the temperature coefficient of frequency of the FBAR material stack (aluminum nitride piezoelectric film with platinum and aluminum electrodes). Least-square fits to a second-order polynomial of FBAR oscillator output spectra as a function of temperature are shown in Figure 10. The temperature coefficient of frequency (TCF) of the FBAR oscillator output spectra is quite constant and typically lies in the range of -24 to -25 ppm per ºC. The TCF is negative because the AlN film softens (elastic modulus decreases) with increasing temperature. Because of variations in FBAR film thicknesses, FBAR and CMOS chip mounting (adhesive), bondwires, etc., before collection of deposited-mass data, the TCF of each FBAR mass sensor must be measured by performing a simple baseline run with no particles.

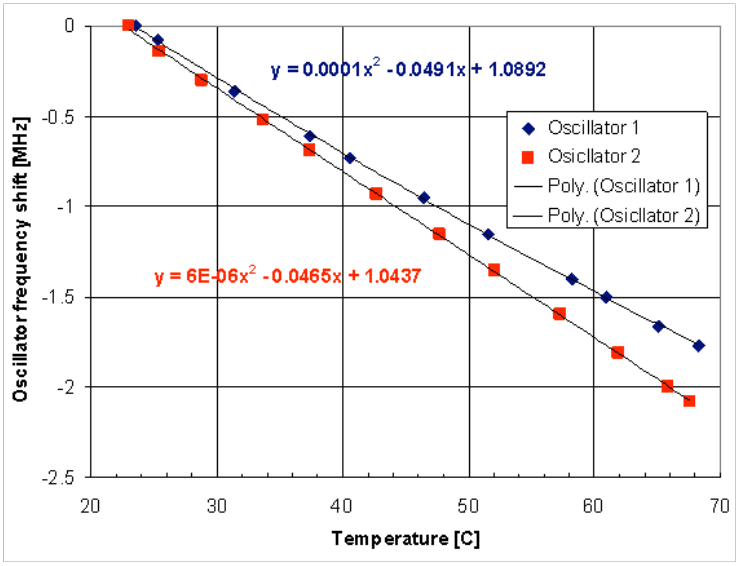

Figure 10. Frequency shifts vs. temperature for two FBAR oscillators. The FBAR mass sensor temperature coefficient of frequency is highly linear.

As shown in Section 3, the temperature fluctuation, if accurately measured, is readily de-correlated from the particle-induced frequency shift. Measurement of the MEMS PM monitor temperature with a commercial off-the-shelf thermocouple, positioned in contact with the monitor housing, has been found to give good experimental results. Further discussion of temperature compensation is found below in Section 2.c.iv.

2.c.iv. Control and measurement equipment

We naturally used conventional laboratory measurement equipment to control our experiments, and to collect and process resultant data. The project did not have sufficient funding or time to proceed to the next step of designing truly appropriate control and measurement equipment for a battery powered portable unit – that was not a specific goal of this project. Such control systems are widely used for sensor applications, and straightforward engineering designs can be applied by a manufacturer who wishes to develop a commercial version of the device. However, significant progress has been toward the long-range goal of designing control and measurement equipment for a battery powered portable unit. This progress is described below, after a brief introduction to the relevant electronics.

The primary obstacles to a portable, battery-powered instrument are down-conversion of the 1.7 GHz FBAR oscillator signal to a MHz frequency range and implementation of a baseband digital signal processor (DSP) for automated data extraction. The 1.7 GHz oscillator output must be demodulated to baseband frequencies (typically tens of MHz) in order to interface with inexpensive digital circuitry. Figure 11 shows a homodyne down-conversion architecture.

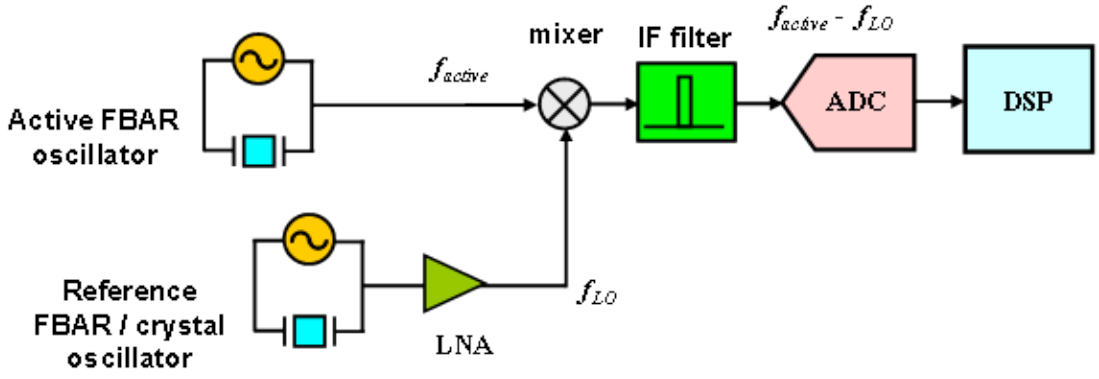

Figure 11. Proposed circuitry to down-convert and analyze FBAR mass sensor data. Acronyms are defined in the text.

In the first step of down-conversion, the active FBAR mass sensor (at a frequency f_{active}) is mixed with a reference FBAR oscillator or ultra-stable temperature compensated quartz crystal oscillator (f_{LO}). In the frequency domain, mixing corresponds to sinusoidal multiplication whereby two new sinusoids are created at frequencies $f_{active} + f_{LO}$ and $f_{active} - f_{LO}$. For example, if $f_{active1} = 1.70$ GHz and $f_{active2} = 1.69$ GHz, a difference frequency is generated at 10 MHz. The original 1.70 GHz signal, higher harmonics, the sum frequency, and any out-of-band noise are removed with the intermediate frequency (IF) filter. The analog baseband signal is subsequently digitized by the analog-to-digital converter (ADC) and processed in the DSP.

Three techniques to down-convert the active FBAR oscillator signal were studied in this project. First, a mixer and two oscillator circuits were designed in a 0.25 μm CMOS process. Figure 12 contains a transistor-level schematic of the mixer and the Cadence™ layout of the entire circuit. The chip was characterized, but unfortunately the mixer did not function properly because of losses in the AC coupling capacitors.

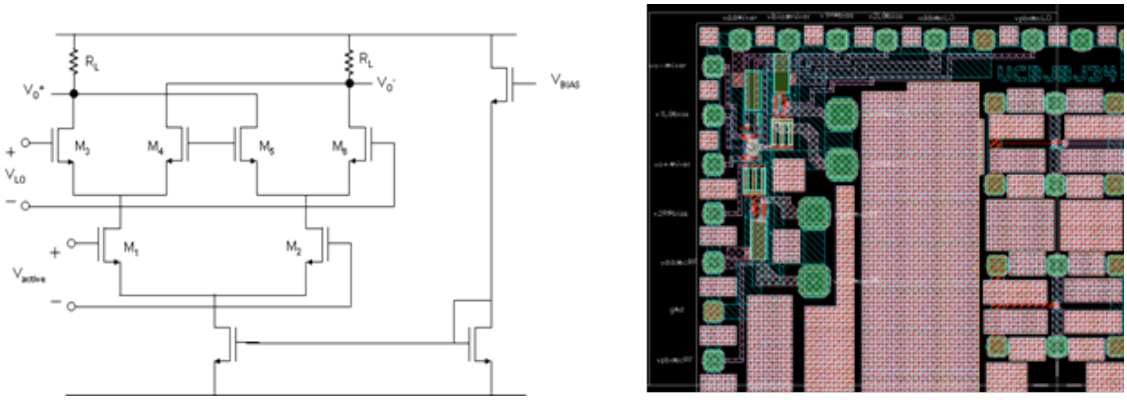

Figure 12. Schematic of CMOS mixer circuit and layout of integrated circuit with active and reference oscillators.

The second method involved the use of a commercial doubly-balanced mixer from Minicircuits (ZX60 – 2522M). The beat frequency of two FBAR oscillators (at ~ 11 MHz), measured with a spectrum analyzer (Figure 13a), was recorded over 8 days. Fig. 13b shows the mixer output spectrum. The FBARs were exposed to ambient temperature fluctuations in a laboratory in the UC Berkeley Electrical Engineering building. Fig. 13c displays the variations of the FBAR signal and the room temperature with time. The results show that the setup did not completely cancel the temperature dependence because the two FBARs had different temperature coefficients.

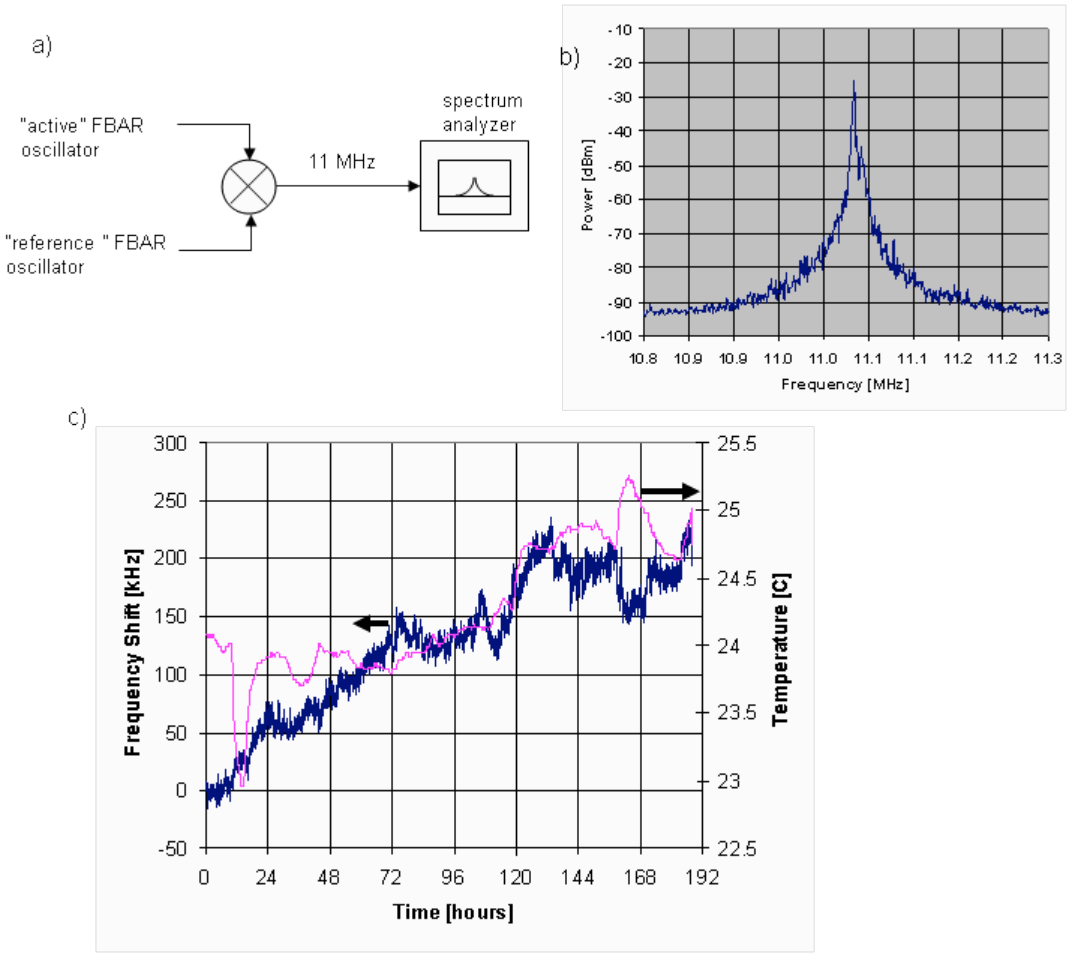

Figure 13. Beat frequency of two FBARS, mixer output, and temperature compensation. (a) The beat frequency of two FBAR oscillators (~ 11 MHz), measured with a spectrum analyzer, was recorded over 8 days; (b) 11 MHz mixer output spectrum; (c) temperature and change in mixer output frequency over eight days.

The third technique used a passive mixing scheme whereby electromagnetic coupling between nearby FBAR oscillators self-mixed to create a difference frequency. The hypothesis was that electrical mixing of the output of a given mass-sensing element with that from a nearby uncoated reference oscillator would largely compensate for the temperature dependences of the mass sensing elements. Self-mixing between the two oscillators occurred because of the nonlinear CMOS transistor gain (the drain current of a CMOS transistor has a square dependence on the gate voltage). This technique encountered the same difficulty as the MiniCircuits mixer experiment – namely a mismatch in the FBAR temperature coefficients of frequency.

Based on results gained obtained during this project, the investigators believe the best approach to demodulate the FBAR signal is to use an off-the-shelf temperature compensated quartz crystal oscillator as the reference oscillator. Quartz crystal

oscillators with 0.5 ppm frequency shift over a 80 ºC temperature swing cost only a few dollars. With measured temperature data at hand, the temperature induced frequency shift in the FBAR can be readily subtracted.

The prototype MEMS PM monitor does not use a reference oscillator. Instead, the TCF was determined for each FBAR by performing a simple baseline run with no particles and with ambient temperature fluctuation. By incorporating the calibration scheme into the DSP module, the FBAR could be automatically corrected in real time for temperature changes.

Resonator saturation due to mass loading is a concern with acoustic resonators. One problem with commercial QCM PM sensors is the frequency with which the crystal surface must be cleaned to avoid signal saturation. This issue exists in theory with the FBAR as well. Therefore, an experiment was carried out to identify the saturation limit of the FBAR. Aluminum was evaporated onto the resonator surfaces of three FBARS in four incremental steps. Each step added about 1.8 ng of material to the surface and caused a corresponding frequency shift. The total mass loading was 7.24 ng on each FBAR. The rate of change of FBAR frequency with mass loading was found to be 4.2±0.3MHz/ng. This response was very linear ($r^2 = 0.998$) with no indication of saturation at the high end of the loading range. The FBAR saturation limit in the aluminum experiment was therefore not observed even at over 7000 times the minimum detection level of 1 pg. Characterization of the extent to which loading with PM may differ from this experiment has not yet been accomplished. An explanation for the difference between QCM and FBAR saturation limits is that the QCM operates in a shear mode, vibrating on an axis parallel to the particle-substrate interface, while the FBAR vibrates in a (trampoline-like) mode perpendicular to the particle substrate interface.

In addition to the apparent high mass-measuring capacity of an individual FBAR, the MEMS PM monitor contains an array of FBAR sensors. These sensors can be switched with loading or for other reasons, multiplying the total loading capacity by the number of sensors available. Furthermore, the microfabricated nature of the FBAR module chip will eventually enable inexpensive replacement of one for another, similar to the SIM chip of the cellular telephone.

Standby loading of the FBAR array on a chip can occur because the sample air passes over all of the sensors on the module chip. The problem is mitigated since particles of significant mass only load on FBARs for which the thermophoretic heater is activated, i.e., those for which measurement is in progress. Ultrafine particles with diameters <~50 nm will load on all surfaces due to diffusion (Ref. 7). However this is not a problem for two reasons: 1) these particles are very low in mass since they are so small, and 2) the MEMS PM monitor is operating on the rate of change of FBAR frequency, not the absolute frequency, so the initial FBAR frequency can be shifted by previously collected particles with no effect on accuracy.

Calibration of the FBAR module for mass sensitivity must currently be carried out for each array. This involves both derivation of a temperature sensitivity curve with no

challenge aerosol, and then a mass sensitivity curve with a challenge aerosol of known concentration. This situation may change in mass production if manufacturing processes are stable and consistent enough so that the temperature and mass sensitivities of these monitors become sufficiently repeatable.

2.c.v. Optical module

As mentioned earlier, the concept for the MEMS PM monitor includes measurement of light absorption by the deposited particles to obtain information about their chemical composition. Figure 14 shows how light reflected from the deposit would be monitored by photo-detectors.

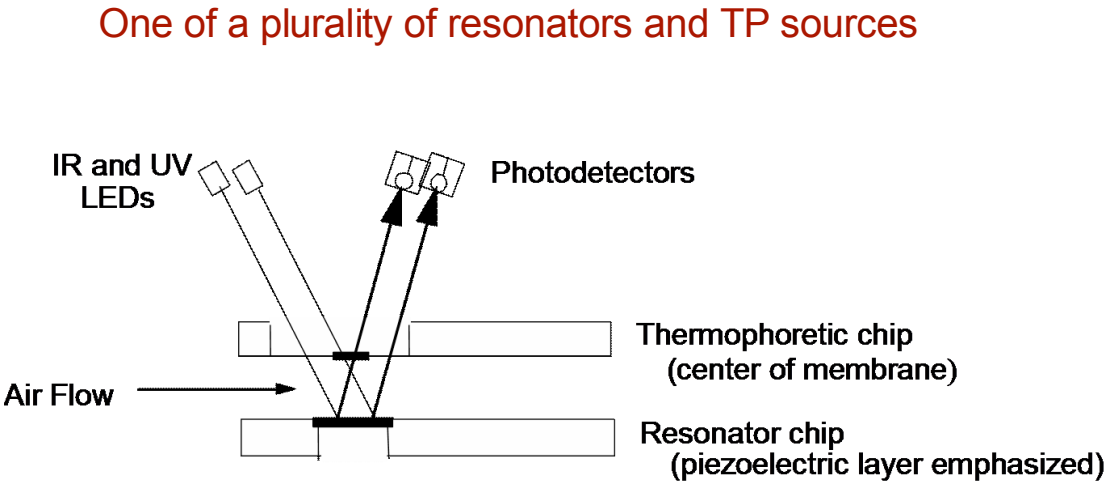

Figure 14. Concept of simultaneous mass measurement and optical characterization of the deposited PM with one resonator mass-sensing chip and a pair of LEDs and photodetectors for optical characterization of the deposited particles.

Prior work at LBNL (Ref. 12) has shown that such optical testing can yield information about the chemical nature of the deposit. Figure 15 shows how data may be obtained from illumination by UV to near IR radiation incident on a deposit, using a miniature spectrophotometer with a fiber optic probe. The change in absorbance depends on the concentration and chemical composition of the deposit, as well as the concentrations of the light absorbing constituents.

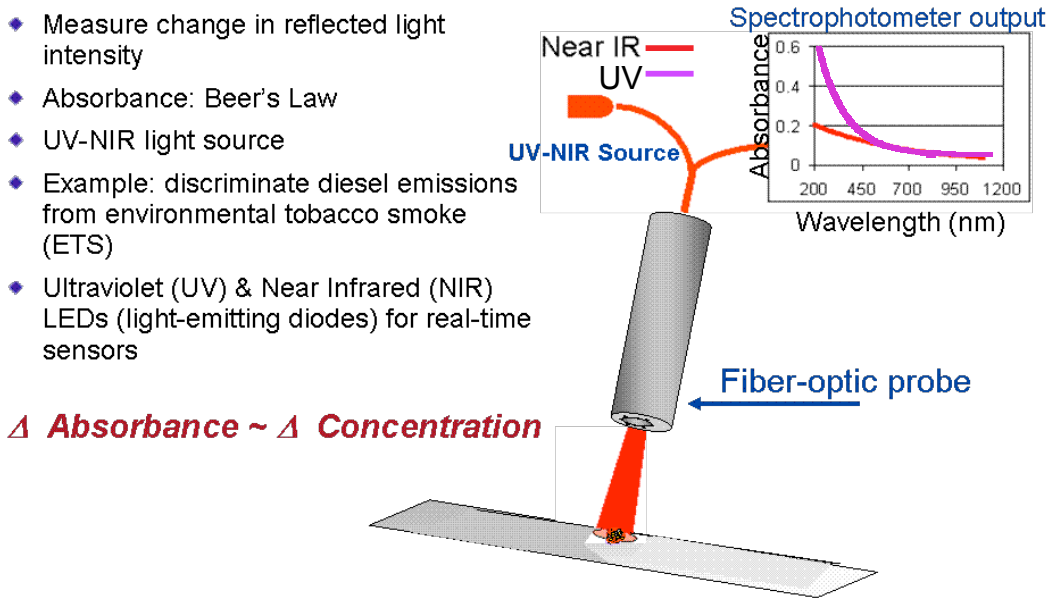

Figure 15. Fiber-optic probing of a particle deposit. The inset at the upper right shows the absorption spectrum of black particles on a deposit. The MEMS PM monitor uses light emitting diodes for illumination and photodiodes for detection.

Figure 16 shows the excellent correlation obtained between the mass of ETS deposits from a succession of cigarettes on the earlier LBNL prototype mass sensor and UV absorbance at 370 nm. Also shown are data from a commercial optical particle counter used as a reference.

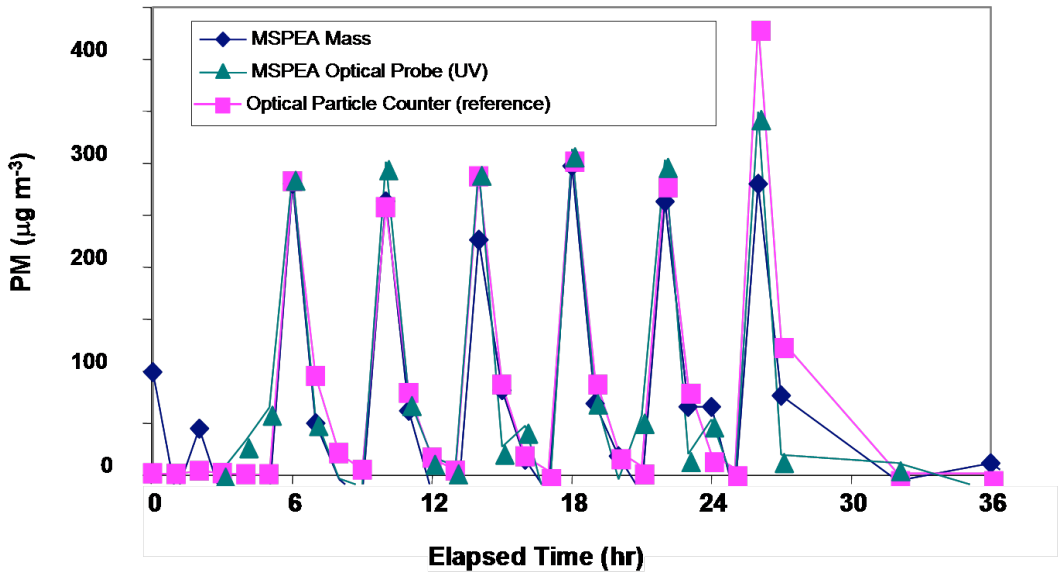

Figure 16. Correlation of optical probe data and mass deposits for successive cigarettes.

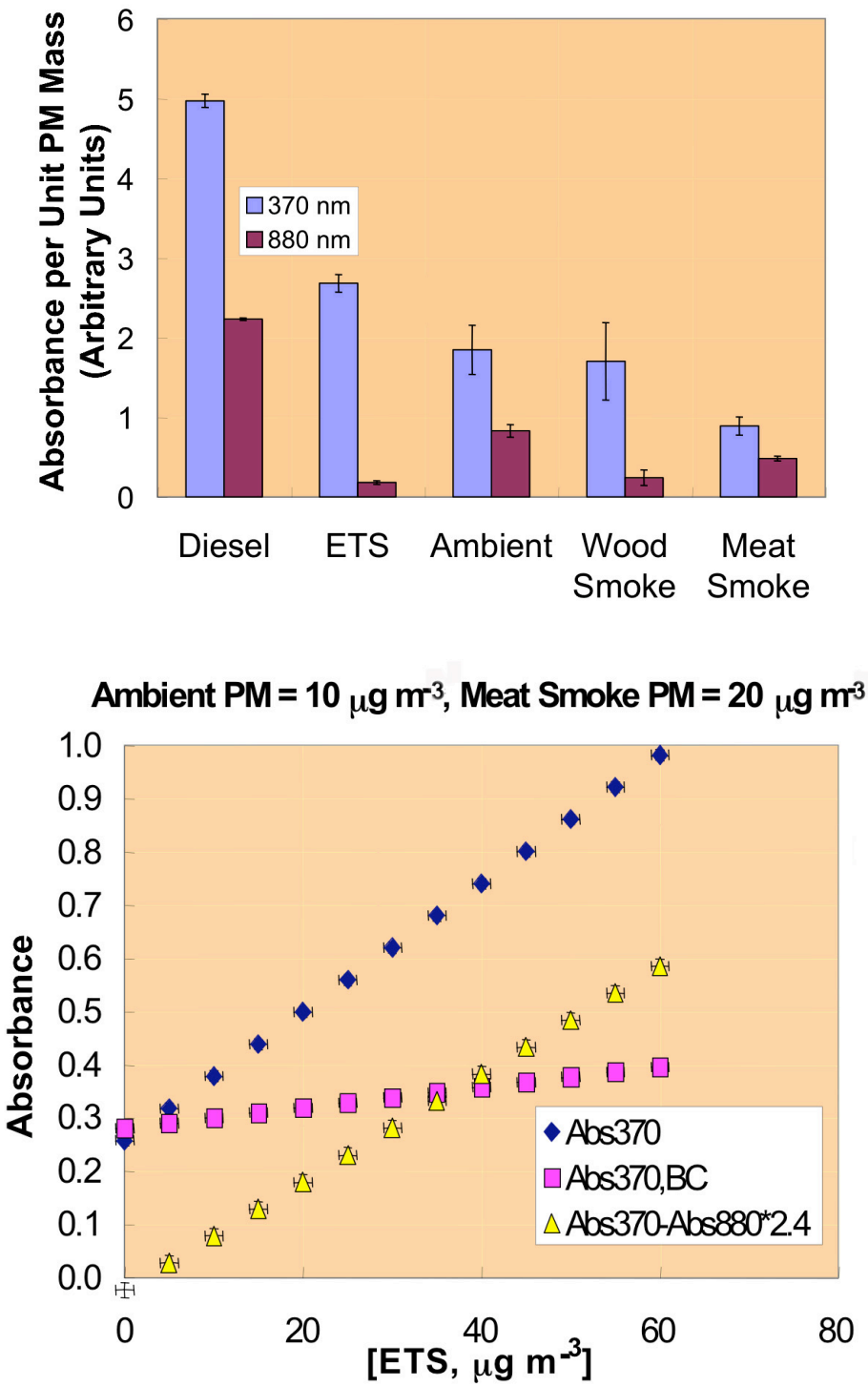

Figure 17. Optical discrimination of particle deposits. ***(Upper Figure)*** **Comparison of absorbances in the near UV and near IR for combustion sources that generate airborne PM. At the center of the chart labeled "Ambient" are absorbances of PM collected in Berkeley, CA.** ***(Lower Figure)*** **The triangles show that the difference between ultraviolet and IR absorbance is proportional to ETS concentration in the presence of ambient PM and meat smoke, based on the relationships shown in the upper figure.**

Using two (or more) test wavelengths can yield information about the chemical nature of the deposits. Fig. 17 shows how particles from a variety of combustion sources absorbed UV and IR light when they were diluted in ambient air in LBNL's environmental chambers (Ref. 12). The y-axis is expressed in units that are proportional to the observed absorption coefficient per unit PM mass for each source in the UV (370 nm) and IR (880 nm). A dual wavelength aethalometer (Magee Scientific) measured the light absorption while particles were also collected on a quartz crystal microbalance (for mass size distribution) and a filter (for PM concentration by gravimetry).

The grey or black appearance of ambient PM is due primarily to the presence of black carbon (BC), and at least 90% of the BC is contributed by the exhaust of diesel engines. BC absorbs light continuously like a black body throughout the UV, visible and IR spectral regions, and its absorption coefficient varies inversely with wavelength. At 370 nm, a black body absorbs 2.4 times more strongly than at 880 nm (880/370 = 2.4). Fig. 17 shows that diesel PM in ambient air absorbed UV at 370 nm 2.3 ± 0.1 times more strongly than IR at 880 nm, indicating that diesel PM absorbs light like a black body. For ambient PM the ratio of UV(370) to IR(880) was $1.9/0.85 = 2.2 \pm 0.3$. The lower half of Fig. 17 gives an example of how the contribution of ETS can be distinguished from indoor particles that originated from outdoor ambient air and meat smoke

We have tested both infrared and ultraviolet LEDs, and both appear suitable for this application. The LEDs are available in chip form, so their dimensions are suitable for incorporation with the other micro-sized elements of the monitor. The IR and UV LEDs have fairly broad directional characteristics, but beam-confining attachments could be used to direct the beams and prevent spill-over of a given beam onto several deposits. The electric power requirements of the IR and UV LEDs are reasonable. In order to reduce the average power dissipation and prolong battery life, the LEDs could be activated intermittently.

An optical printed circuit board (PCB) module consisting of a Hamamatsu 5-element photodiode (S6840) and UV (395 nm) and IR (810 nm) LEDs was designed, assembled, and tested (see Figure 18). A key advantage of this particular make of photodiode was its spectral sensitivity to both UV and IR light. The geometry of the four-element FBAR array was designed to align specifically to the photodiode array, with one FBAR per quadrant (the fifth centered, photodiode element was not specific to any one FBAR).

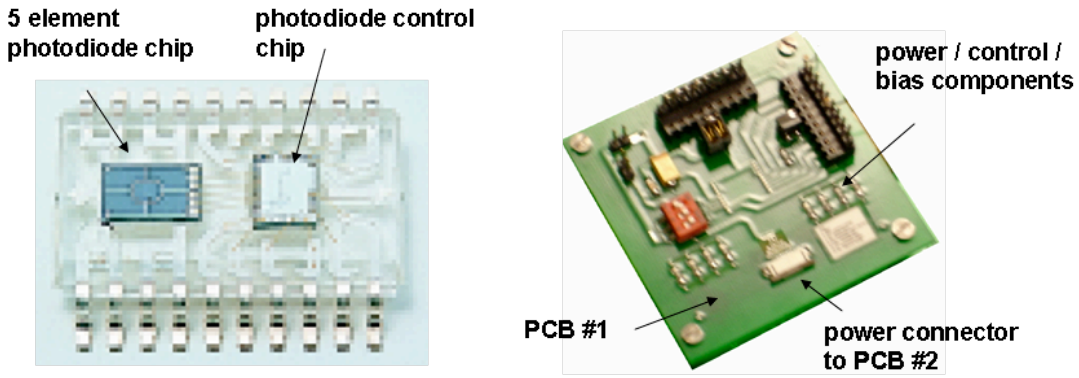

Figure 18: Optical module components. (a) Photograph of optical module (PCB #1); (b) Hamamatsu S6840 photodiode with 5-element sensor array.

As shown in Figure 19, PCB #1 supports the photodiode and control electronics, all soldered surface mount components. A second, thinner PCB (#2) was carefully aligned to the photodiode and attached with glue. As seen in the figure, PCB #2 had a window cut into, which aligns to the photodiode chip, as well as pads and electrical traces (anode and cathode) for 300 µm x 300 µm x 500 µm UV and IR LEDs. The UV and IR LEDs were attached with conductive epoxy. The inset perspective viewshows the 5-element photodiode array through the window in PCB#2.

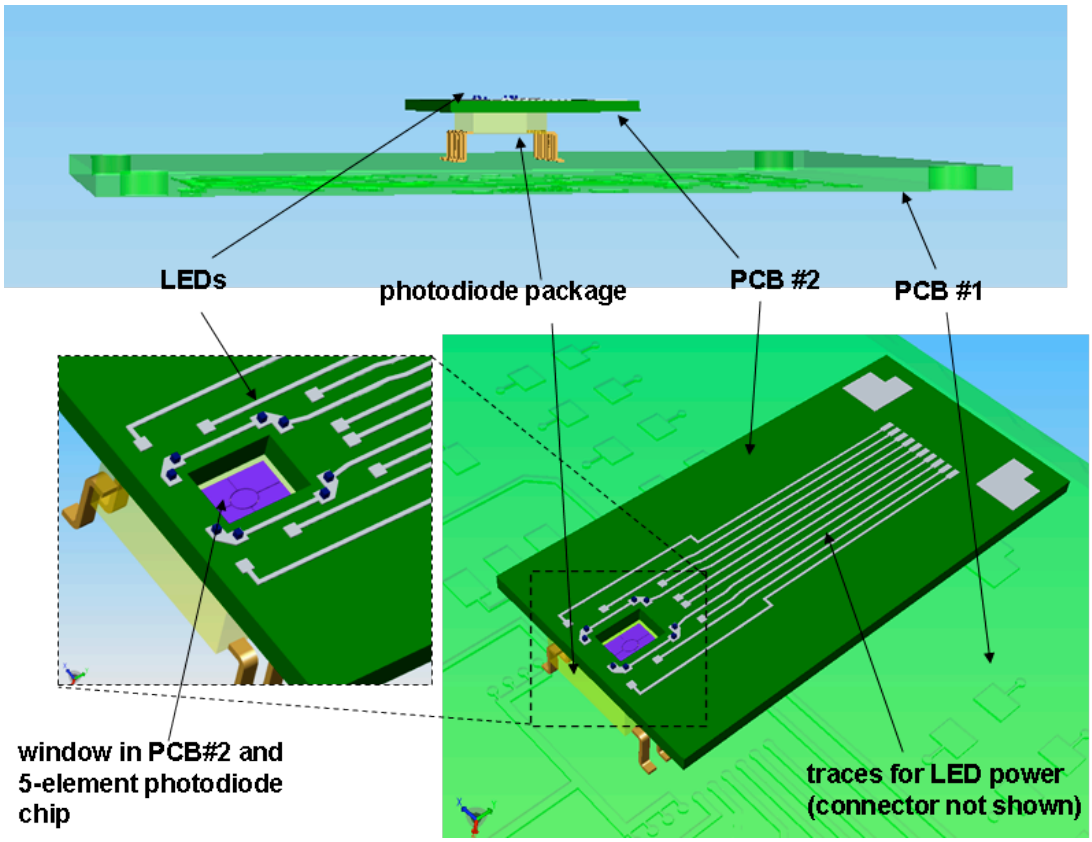

Figure 19. Side and perspective views of the optical module (created using Solidworks).

In principle, light emitted from the LEDs reflects off the FBARs and returns through the window in PCB #2 to be measured by the photodiode. To establish a baseline for operation of the optical module, it was first tested using ETS films deposited onto a highly reflective aluminum surface. The reflective surface consisted of 200 nm of aluminum evaporated onto a silicon wafer. A linear array of ETS test patterns was formed by pipetting ethanol with dissolved ETS onto the aluminum coupon and allowing the ethanol to evaporate. As shown in Figure 20, the window in the optical module was positioned 2 – 3 mm above the aluminum coupon with a micromanipulator. The LEDs / photodiode source – detector was linearly scanned across the ETS test patterns (out of the page) while monitoring the photodiode output voltage. In this test, the photodiode output voltage was expected to exhibit a spatial dependence that correlated with the position of the ETS test patterns.

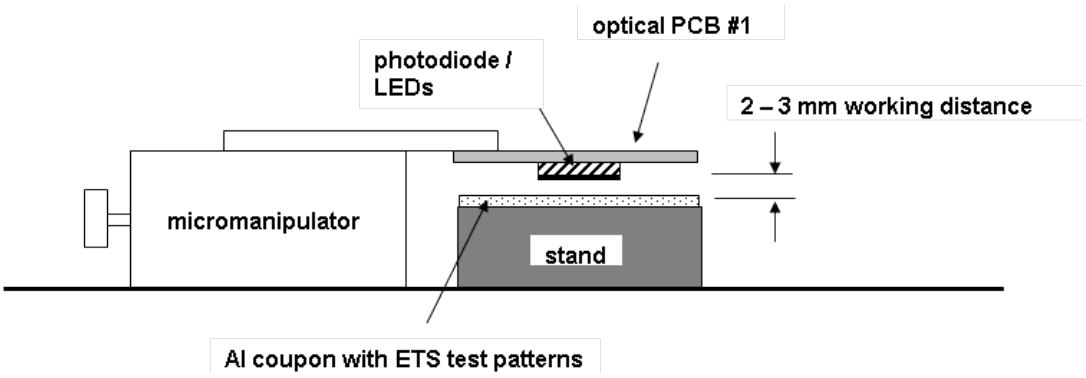

Figure 20. Test setup for calibrating the optical module

Testing showed that light scattered from surfaces of the test fixture and transmitted through PCB #2 overwhelmed the signal reflected from the aluminum coupon and the ETS film. Extensive efforts with an AC LED-drive and lock-in-amplifier detection scheme to cut down the noise due to scattering were not successful. We found that because the LEDs produced quite broad beams of radiation, there was significant light scattering from surfaces other than just that of the FBAR where the particles deposited. An attempt to coat all surfaces with light-absorbing black paint also proved unsuccessful. Therefore, the optical components of the assembled MEMS PM device were not activated for further testing in the environmental chamber or field study.

2.c.v.1. Additional optical experiment: Using transmission rather than reflection

We have identified several ways of solving the problem just described. Promising preliminary results were obtained with an alternative configuration in which PM deposition would occur on a thin layer of quartz (or glass since UV absorptive losses are negligible during transmission through very thin glass layers) just above the surface of the LEDs (in the same plane as the FBAR) for measurement by direct optical transmission rather than reflection. In this configuration, a much higher fraction of the light reaching the photodiode passes through the PM deposit.

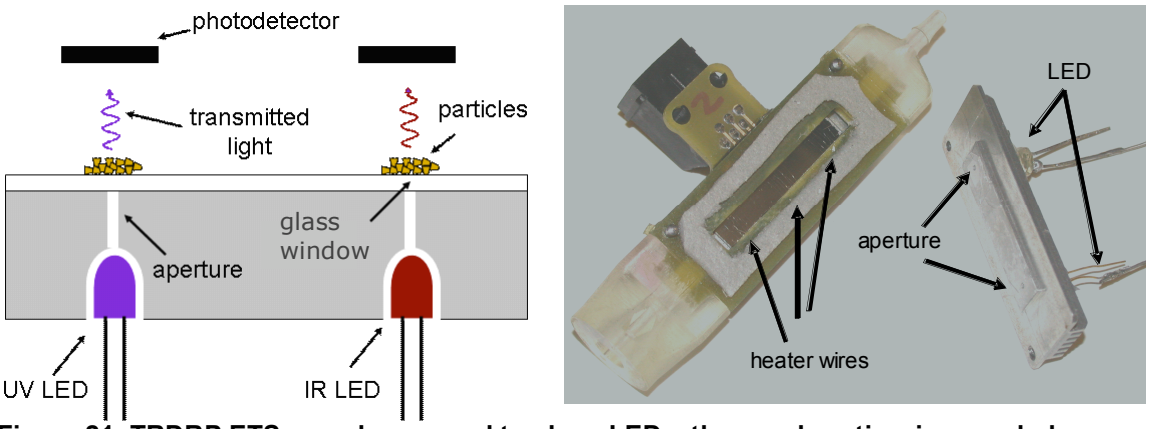

Figure 21. TRDRP ETS sampler opened to show LEDs, thermophoretic wires, and glass and aluminum collecting surfaces.

A series of experiments that inform on this alternative configuration was conducted at the very end of this ICAT project. The experiments made use of a modified thermophoretic ETS sampling assembly developed for the TRDRP. As shown in Figure 21, the apparatus for collecting particles consists of a loom-like frame machined from a copper-clad printed circuit board that holds a set of TP wires and acts as a flow channel, plus a mounting surface for fin-cooled aluminum particle collection plates. When assembled, the device becomes an air-tight flow-through channel with three sets of TP collection areas; a small pump (10 cm^3 min^{-1}) was used to draw a PM-laden air sample through the device. Four fine TP wires (California Fine Wire Co., nickel alloy 120) 25 μm in diameter and about 5 mm in length were soldered, physically in parallel and electrically in series, to form a coplanar resistive heater on the collector frame about 5 mm on a side. Three of these heaters were assembled on a single sampler to create three separate TP collection regions (see Figure 21). When the TRDRP sampler was assembled and a voltage was applied across one of the three wire circuits, a thermal gradient was formed between the wire and the fin-cooled aluminum collection plate.

An optically transparent glass collecting surface was assembled with a thin (about 200 μm) glass cover slide attached to the collection substrate of the aluminum collection plate body. The glass cover slide was glued at edges to allow light transmission through two circular ~1 mm-diameter pinholes. UV- and NIR-emitting LEDs (380 and 810 nm, respectively) were inserted into the back of the aluminum body, allowing light beams to be transmitted through the pinholes and emerge normal to the glass surface. The LED pinholes were located in the centers of the TP deposition surfaces for two of the three collection areas on the glass-covered collection body. A second aluminum body with a reflective surface (not glass) formed the cover on the opposite side of the ETS sampler. (ETS was also collected and measured on this side using reflectance, but these data will not be discussed here.) Figure 21 shows the TP ETS sampler with the LEDs embedded on the sampler cover, and the opposite side with the aluminum cover.

ETS particles were collected at the TP deposition locations on the glass collection surface during cigarette smoldering experiments in a 24 m^3 chamber. A standard test condition was used in which eight cigarettes were smoldered simultaneously in the sealed chamber

and the ETS concentration was allowed to decay over about 17 hours. A gravimetric $PM_{2.5}$ filter sample was also collected at a sampling rate of 2 L min^{-1} for exactly the same time period.

After sampling, the assembly was taken apart and the change in absorbance of light emitted from the embedded LEDs due to ETS loading on the glass surface was measured with a UV-NIR spectrophotometer (Ocean Optics). The light intensities from the LEDs were first measured three times with the ETS loaded (intensity I) on the surface of the glass, and then measured again after the ETS was cleaned off (intensity I_0). Absorbance, A, is proportional to the negative log of the ratio these intensities:

$$A = -\ln (I/I_0).$$

According to Beer's Law, all other parameters being unchanged, the concentration of ETS on the glass collection surface is proportional to the absorbance of the material on the surface. The 380nm and 810nm absorbances were calculated for each ETS sample on the glass collection surface.

The purpose of the experiments was to study the relative deposition of ETS particles as a function of TP gradient as the voltage on the TP wires was varied. However, the data also inform on the use of the optical transmission method proposed above as an alternative to reflection for the MEMS device. TP collection was measured in duplicate experiments with wires operated at 1.0, 1.5, 2.0, 2.5, and 3.0 volts, corresponding to temperatures of approximately 90, 150, 210, 290, 370 ºC, respectively. The UV absorbance at 380 nm, normalized using the $PM_{2.5}$ measurements to a 10 μg sample to correct for small variations in ETS concentrations across experiments, was studied as a function of wire voltage (Figure 22).

An 880 nm LED optical path was also tested in the same experiments, but the results were extremely poor (low absorbances, resulting in imprecise data). This is because of the low absorbance of near infrared light by ETS, relative to that of UV, as shown in Figure 17.

The UV results suggest that the proposed use of absorbance as an alternative to reflection would enable one to quantify the amount of optically absorbing material thermophoretically deposited in a light path. This method may be an option for inclusion of the optical component of the MEMS PM monitor in subsequent designs. Note also in Fig. 22 that the mass deposited on the TRDRP sampler was rather sensitive to TP wire temperature, with a possible peak collection efficiency for a wire temperature around 300 ºC.

2.c.v.2. Optical measurement of TP deposition vs temperature

In addition to its relevance to the optical particle discrimination design, this work indicates that, as expected, selection of the optimum TP heater temperature is key to maximizing the sensitivity of both mass and optical functions of the device. Although

there are some basic differences in the geometries of the TRDRP TP collection system and that of the MEMS PM monitor, it is clear from these data that experiments must be conducted in the future to ensure that the TP deposition efficiency is optimized for the MEMS PM monitor.

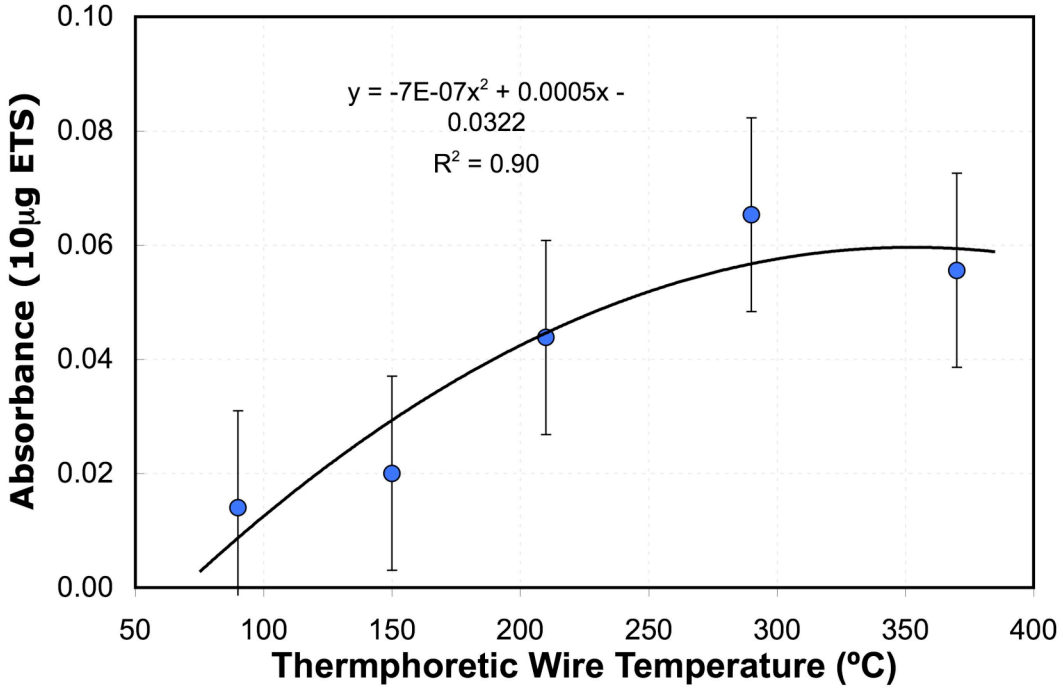

Figure 22. Ultraviolet absorbance of ETS particles thermophoretically deposited onto a 0.2 mm collecting surface in a TRDRP ETS sampler as a function of thermophoretic wire temperature. The UV absorbance was measured using a UV LED embedded in the sampler cover body with its light output beam directed through the ETS sample to a fiber optic input to a spectrophotometer. The absorbance was calculated from the change in UV signal intensity from the glass slip when clean vs. when it was loaded.

3. Results of performance tests

3.a. Environmental chamber studies

This section focuses on the performance of the MEMS PM monitor whose components were described in Section 2. Section 3a describes the device development when we conducted tests in a room-sized chamber at LBNL. The challenge aerosol was typically environmental tobacco smoke in ambient air, although some preliminary experiments sampled diesel exhaust. Section 3b describes the results of pilot-scale field test that took place in a single-family house in Berkeley over two ten-day periods in the early summer of 2006. Section 3c summarizes the test results.

3.a.i. Environmental chamber and its instrumentation

The 24.7 m^3 environmental chamber at LBNL had vinyl flooring and walls of painted gypsum board. The chamber was equipped with a ventilation system, and sensors for real-time monitoring of pressure, temperature, and relative humidity (RH). More information about the chamber is found in Ref. 13.

The following suite of instruments was available for concurrent PM monitoring and FBAR data acquisition during the chamber experiments:

Quartz crystal microbalance impactor (QCM) with 10 impaction stages and size cuts of 0.05, 0.1, 0.2, 0.4, 0.8, 1.6, 3.2 and 6.4 μm (California Measurements, Model PC-100) for PM mass size distribution (μg m^{-3}), with customized measurement circuitry and laboratory-built control and data acquisition software. The QCM was operated at a flow rate of ~240 cm^3 min^{-1}, and was typically programmed to start and continue sampling until a pre-selected frequency change was reached for the 0.2 μm stage. The QCM was programmed to restart a new cycle if the pre-set mass loading had not been reached before 30 min.

Optical particle counter (OPC) with 6 channels for particle number size distribution (# m^{-3}), with size bins 0.3, 0.5, 0.7, 1, 2 and 5 μm (Met One, Model 237B). PM concentration was calculated from these data by summing the product of the estimated average particle volumes in each size bin and the number concentration in that bin. The total particle volume was based on estimated diameters of 0.358 μm, 0.56 μm, 0.81 μm, 1.43 μm, 3.16 μm and 7 μm for the 0.3, 0.5, 0.7, 1, 2 and 5 μm bins, respectively. A particle density of 1 g cm^{-3} was assumed. For an estimated PM 2.5, bin volumes for the lower 5 bins were multiplied by the counts for those bins, and the upper bin was excluded. This volume sum was multiplied by 1 g cm^{-3}.

Aethalometer, for black carbon concentrations (μg m^{-3}), by attenuation of light at 880 nm, and BC-equivalent concentrations at 6 other wavelengths (Magee Scientific, Model AE-42) customized at LBNL with LEDs at 370, 430, 470, 520, 590, 700 and 880 nm; operated at 2.4 L min^{-1} with one minute reporting periods.

Filters for PM mass concentrations of ETS or diesel exhaust particles over short intervals (hours) at 30 L min^{-1} using Teflon-coated glass fiber filters, 47 mm in diameter, equilibrated for 24 hr at 38% RH before weighing on an electronic microbalance. This instrumentation produced a measurement that we are defining as PM_{grav} whose units are μg m^{-3}.

Pumps and flow measurement devices (bubble meters and electronic flow meters).

Chamber for 24-hr equilibration of filters at RH of 39±1% at 70-72 ºC.

Microbalance (±1 μg) for gravimetric determination of PM mass collected by filters (Cahn Automatic Electrobalance, Model 21); and

Spectrum analyzer (Hewlett-Packard Model 8562EC) for monitoring FBAR frequency.

3.a.ii Generation of challenge aerosols

ETS from a popular brand of cigarette was generated inside the environmental chamber by an automated smoking machine (built at LBNL) that could light, burn and extinguish up to 16 cigarettes, sequentially, one at a time, under computer control. The smoking machine was connected to a pump (A. D. Little, Inc.) that drew 35 cm^3 of mainstream smoke once a minute, using a puff profile that simulated human cigarette smoking. The mainstream smoke was ventilated outside the chamber.

The QCM and OPC were located in the chamber with the FBAR or the assembled MEMS PM monitor during most of the experiments in which ETS was the challenge aerosol. The chamber was closed and not ventilated until at least 15 hr after the cigarette smoking ended. Other work with ETS in an adjacent chamber (Ref. 14) and in the same chamber (Ref. 12) had shown that the mass size distribution of ETS peaked between 0.1 and 0.2 μm immediately after emission, and that there was never appreciable mass above 1 μm as the ETS aged and deposited on the chamber surfaces. Similar size distributions were observed in this project. The results also showed that infiltration of ambient PM into the chamber was very slow, as expected for a sealed, unventilated chamber. Therefore, during the chamber experiments, a $PM_{2.5}$ size-selective inlet was not used for the FBAR, MEMS PM monitor, or filter sampling.

Near the end of the project, an experiment used diesel smoke as the challenge aerosol. Fresh diesel exhaust was admitted to the chamber through a dedicated 5-cm-diameter supply line that tapped a portion of the undiluted exhaust from a portable diesel-powered generator (Acme Motor 80X-300) that operated outside the building. The system was designed to generate steady diesel exhaust concentrations under reproducible conditions: A small blower drove the exhaust into the chamber while ambient air was supplied to the chamber through the ventilation system. The amount of dilution and extent of equilibration of the diesel PM were not measured directly. During this experiment, the QCM and OPC acquired particle size distributions and PM was collected on filters for gravimetric determination of PM concentration.

3.a.iii Proof of concept for PM mass sensing on an FBAR

Progress in developing of the MEMS PM monitor can be tracked by comparing mass sensing data from chamber experiments in 2004 and 2006. Fig. 23 shows the FBAR

response from an experiment in 2004 plotted as the time derivative of resonant frequency (right axis) and inferred particle mass concentration (left axis).

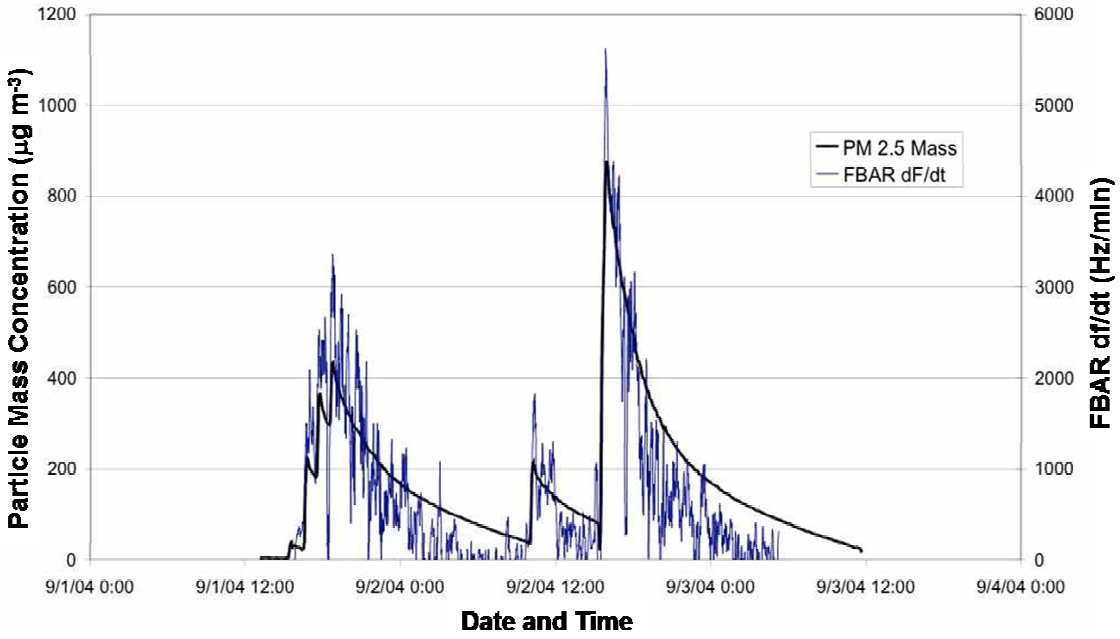

Figure 23. Early test data (2004) for an FBAR exposed to smoke produced by several cigarettes. See text for details.

The data of Figure 23 were taken with an aluminum nitride FBAR manufactured by Agilent, Inc.; all subsequent FBAR data were taken with aluminum nitride FBARs manufactured in the UC Berkeley Microfabrication Facility. The FBAR was mounted on a 0.25 μm process CMOS chip that was in turn glued (with cyanoacrylate) under the heating wires in the middle of the channel of the holder built for the TRDRP ETS monitor (Ref. 15). A special printed circuit board was designed with cutouts to align it to the TRDRP holder. Bond pads at the edge of the board interfaced electrically with the oscillator. There was an extra spacer to provide vertical clearance for the cover to which the heater wires were attached. ETS was sampled through the channel at 15 cm^3 min^{-1}. The limit of detection for PM in ETS was about 75 μg m^{-3} at this flow rate. Six cigarettes were smoked over a two-day period: two on the afternoon of the first day, then one in the morning of the second day, followed by three in the afternoon. The PM concentration was derived from the OPC data as described in Section 3.a.i. The y-axis on the left side shows the scale for the OPC data in Fig. 23, and the right side has the y-axis label for the FBAR data. Fig. 23 shows that the OPC and FBAR generally varied together, but the FBAR data were quite noisy.

3.a.iv. Identifying and addressing challenges

One challenge was handling the temperature dependence of the FBAR resonant frequency; this was described in Sec. 2.c.iv. Another identified problem was reducing the sensitivity of the FBAR to mechanical vibrations in the test space. This was handled

by shock-mounting the device. Extraneous electrical pickup was greatly reduced by shielding the connecting wires.

The final challenge was processing the FBAR signals to obtain mass information, which we will now describe.

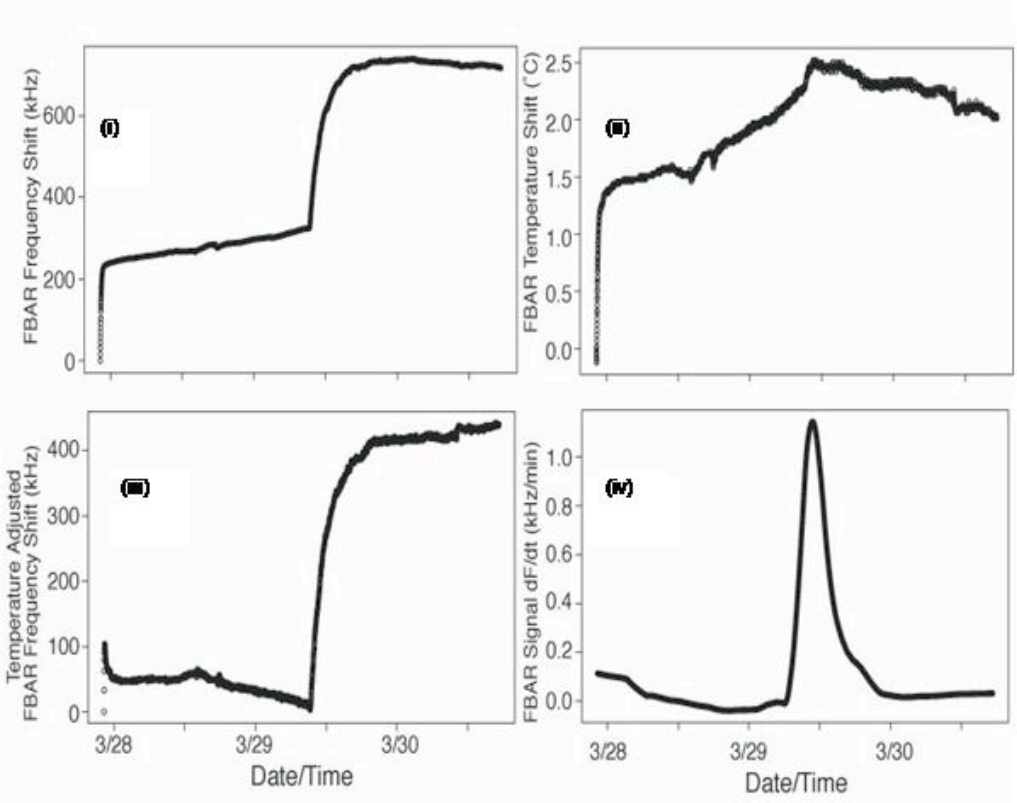

Figure 24. Procedure for extracting temperature-compensated df/dt data from FBAR frequency signals and the ambient temperature log. (i) Upper left: frequency vs date/time; (ii) Upper right: temperature shift vs date/time; (iii) Lower left: frequency signal after subtracting the temperature dependent component; and (iv) Lower right: time derivative of frequency vs date/time, after use of the R-language Supersmooth algorithm.

Figure 24 shows the data-processing procedure developed in 2006 to extract temperature-compensated df/dt data from the real-time frequency signals of the FBAR sensor in the MEMS PM monitor, illustrated for data collected during and after a chamber experiment with one cigarette. Data were processed using the R language (www.r-project.org). Raw FBAR date/time and frequency pairs were read into an R vector (plot i). Likewise, raw FBAR date/time and temperature pairs became an R vector (plot ii). The temperature coefficient of frequency (TCF) of 57.8 kHz/^{o}C was derived in the laboratory by measuring the frequency shift of the FBAR with the thermophoretic heater on, in the absence of particles (sampling pump off). FBAR frequency data were temperature adjusted (plot iii) by subtracting the temperature-related frequency component

(temperature shift x TCF) from the measured frequency shift. The derivative of the FBAR signal with respect to time, df/dt, was calculated by dividing measured time steps into measured frequency steps. The derivative was processed through a smoothing algorithm (Supersmooth with 10% span, R language). The output data appear in (plot iv).

3.a.v. MEMS PM monitor response to ETS

Measurements were made in the room-sized environmental chamber in 2006 after a number of improvements were made in the MEMS device. As noted above, sources of mechanical noise had been largely eliminated by shock-mounting the device, pickup of electrical noise was greatly reduced with shielding, and signal processing of the mass sensor output was done to smooth the data.

Initial tests were conducted with the QCM as a reference to determine whether the FBAR output was tracking the ETS concentration profile in the environmental chamber. The QCM was used in an un-calibrated mode simply to look at relative changes in chamber concentration. After we established that the prototype device was responding with a signal that changed in proportion to chamber particle concentrations, experiments were done to derive a calibration response factor for converting time derivative of FBAR frequency to concentration. These later calibration experiments were conducted with multiple gravimetric filter samples as a reference.

Figure 25 shows the processed FBAR data plotted with data from the co-located uncalibrated QCM that operated during collection of the data illustrated in Fig. 24. The sampling flow rate through the MEMS PM monitor was 1.5 cm^3 min^{-1}. QCM data can be used to convert the FBAR response to PM concentrations, as shown below. It is not presently known whether the apparent lag in FBAR response, compared to the QCM, is real or is an artifact. Since the QCM was operated in an uncalibrated mode, its concentration data are shown relative to the peak concentration. The value of this experiment is that it established that the FBAR response was proportional to a PM mass signal. It did not provide any calibration information for the MEMS PM monitor.

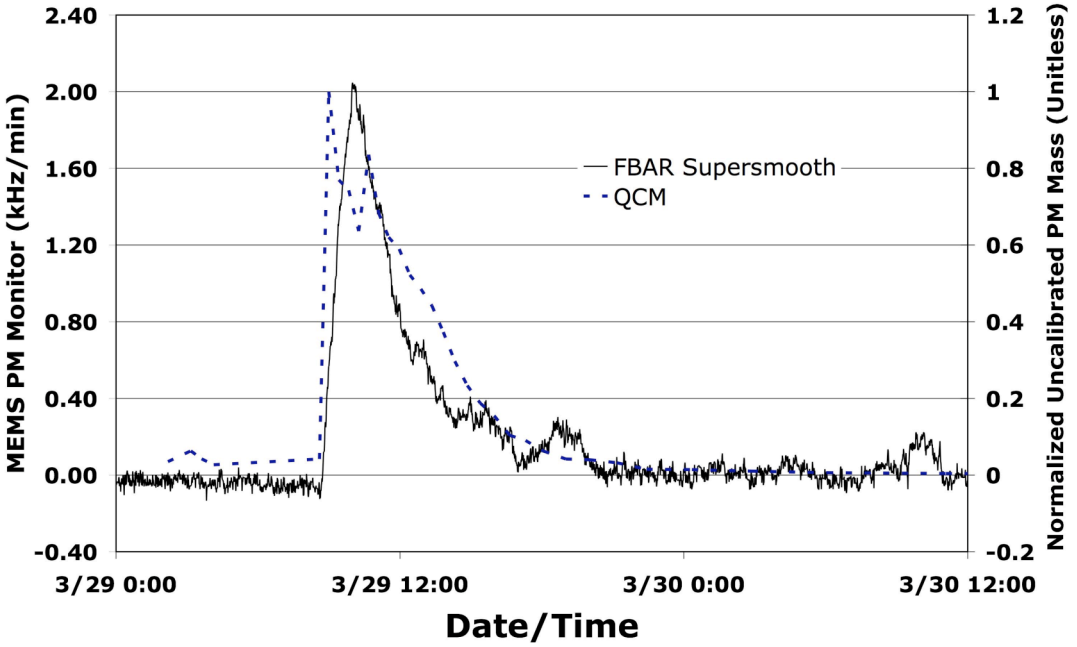

Figure 25. Response of improved FBAR oscillator in the MEMS PM monitor, taken in March 2006, to ETS from one cigarette, along with normalized, uncalibrated QCM mass-sensor data. Time derivatives of sensor resonant frequencies are proportional to real-time concentrations.

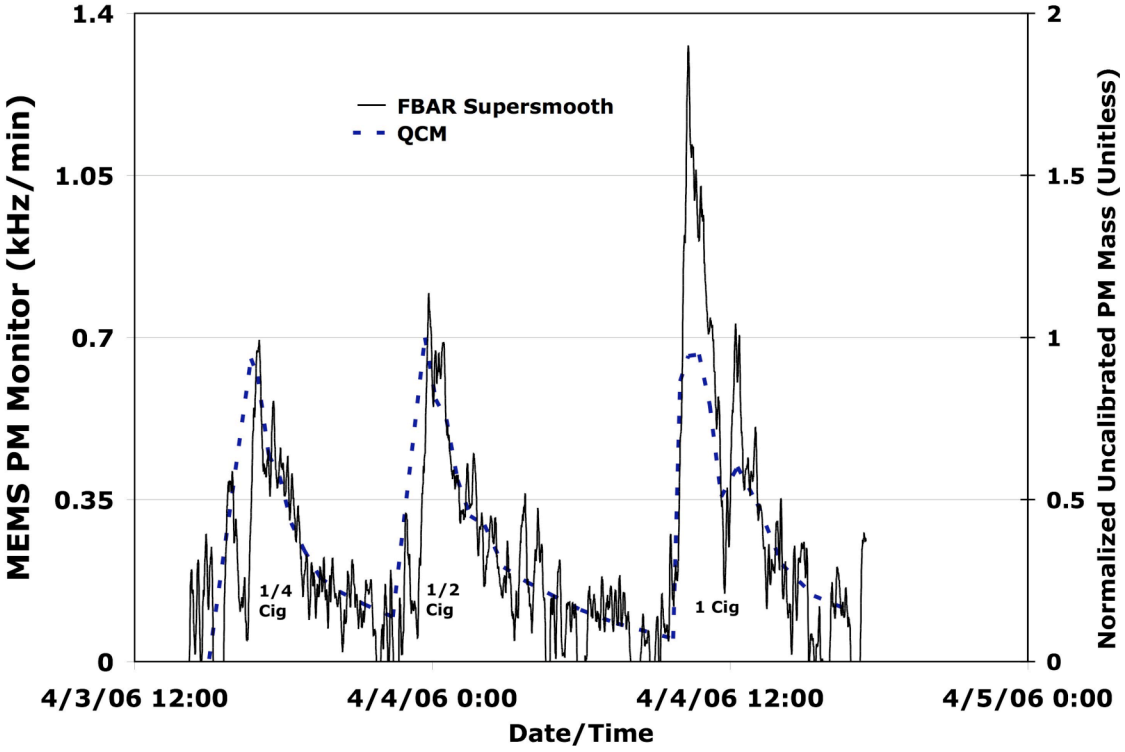

Figure 26. Response of the MEMS PM monitor to smoke from one-quarter, one-half and one cigarette, agreeing with profile from normalized, uncalibrated QCM mass-sensor data.

Fig. 26 shows data from the MEMS device and QCM for PM from smoking ¼, ½ and 1 cigarette in the environmental chamber. Figures 25-26 show that the MEMS PM monitor and QCM generally tracked each other, with some experimental uncertainty, when ETS was the challenge aerosol in the 24 m^3 environmental chamber. Note that the peak QCM data for one cigarette appear to report low relative to the ¼ and ½ cigarette data. The reason for this is unknown, but it may simply be that the QCM instrument was beginning saturate at that point in the experiment. Gravimetric calibration was used in subsequent experiments.

The MEMS PM monitor mass response was calibrated with ETS by relating it to PM mass concentrations that were determined gravimetrically (PM_{grav}) from sampling ETS over short intervals on two Teflon-coated fiberglass filters in series (Figure 27). The method for PM_{grav} was adapted, for sampling ETS and diesel exhaust in the LBNL environmental chamber, from the Federal Reference Method (Ref. 16). The differences were: (1) sampling over periods of several hours, rather than 24 hr, (2) not using a $PM_{2.5}$ size-selective inlet because ETS does not generate particles as large as 2.5 μm, and the ambient PM contribution to the total PM in the chamber was negligible during the experimental work with ETS, and (3) using a second filter inline because the filter manufacturer's information indicated that 5% of particles of 0.3 μm diameter and smaller penetrate, and the mass median diameter of ETS is ~0.2 μm.

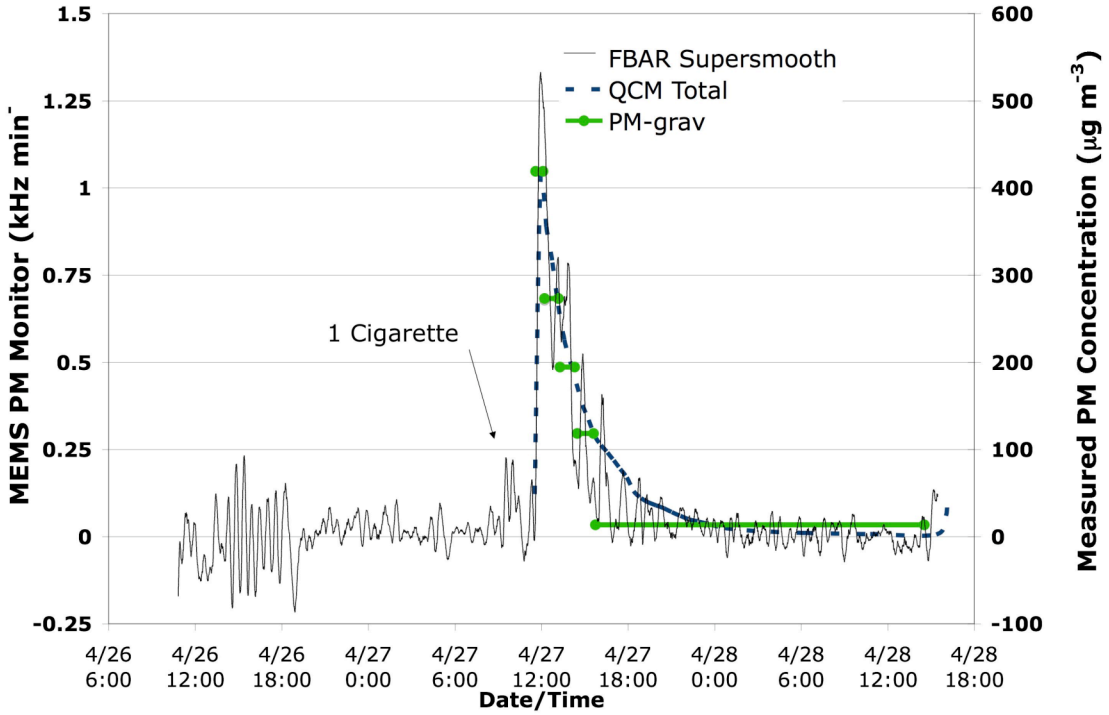

Figure 27. MEMS PM monitor response to ETS from one cigarette, along with PM concentrations from the calibrated QCM and weighed filters (PM_{grav})

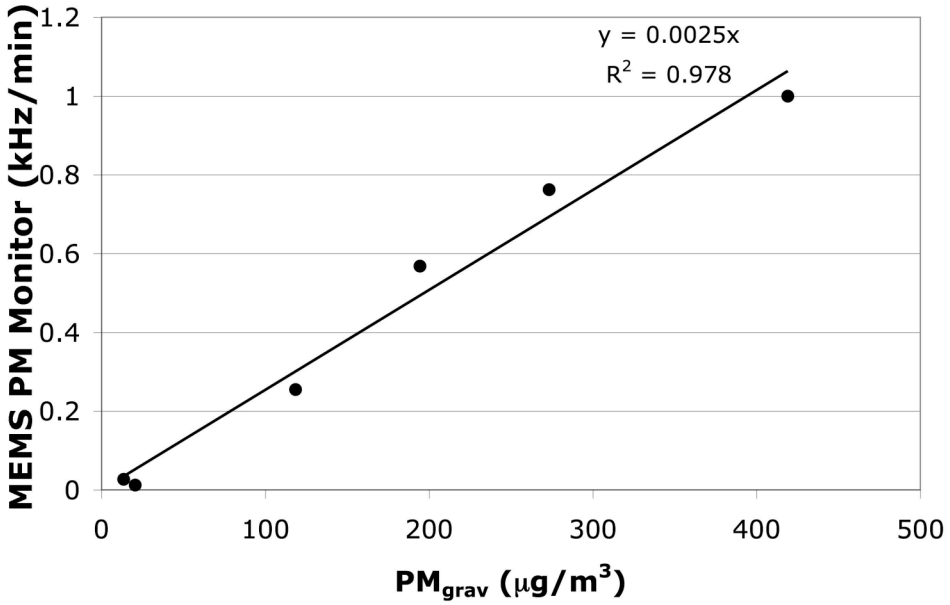

Figure 28. Calibration of MEMS PM monitor based on environmental chamber tests. Relationship between the time derivative of the FBAR signal and PM_{grav} for the data shown in Fig. 27.

The resulting calibration of the MEMS PM monitor (Fig. 28) showed that the temperature-compensated df/dt signal of the FBAR mass sensor, integrated over the same time periods as the filters, was indeed proportional to $PM_{grav,}$ up to $PM_{grav} > 400$ μg m^{-3}. The calibration factor based upon these data is 400 μg m^{-3} per kHz min^{-1} change in FBAR frequency.

3.a.vi. MEMS PM monitor response to fresh diesel exhaust

Generation of diesel exhaust was described in Section 3.a.ii. The environmental chamber was not ventilated while the generator operated (with no load) for 24 min, starting at 15:51 (Fig 29), nor for the next two days. Gravimetric sampling started right before the generator was turned on. The 3-hr average PM_{grav} concentration from filters was 427 μg m^{-3}. Over the same period the concentration of black (elemental) carbon ranged from 430 to 120 μg m^{-3}, as measured by an aethalometer. The 0.05 and 0.10 μm stages of the QCM overloaded after its first measurement cycle, leading to underestimation of the mass concentration by the QCM.

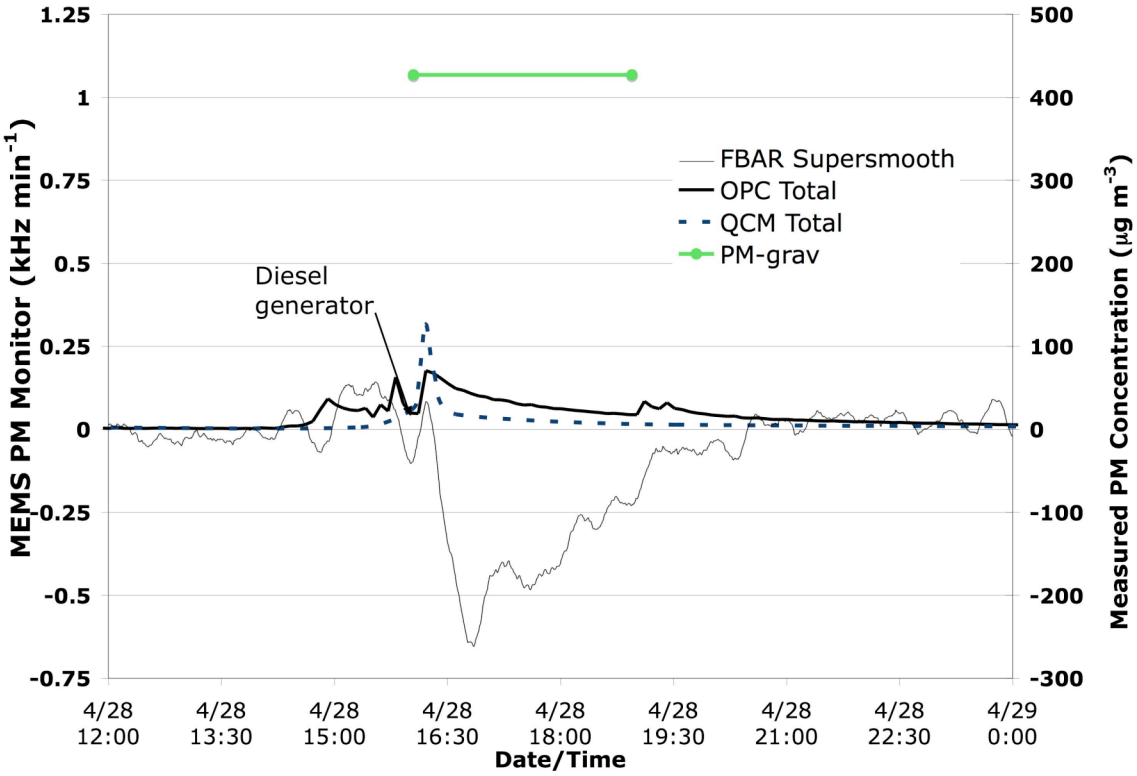

Figure 29. MEMS PM monitor response to fresh diesel exhaust in the environmental chamber, along with data from the OPC and QCM.

Figs. 29 shows that the MEMS PM monitor responded to diesel exhaust when it was added to the environmental chamber, but within an hour the FBAR sensor showed an anomalous response – the resonant frequency rose as the deposited mass increased. One reason may be the following: under normal operating conditions, the impedance between the FBAR electrodes is purely capacitive, and so no DC current can flow from one electrode to the other. However, when conductive particulate matter such as diesel exhaust deposits near the FBAR, a finite resistance appears between the FBAR electrodes. The value of this resistor, which is in parallel with the FBAR, depends on the thickness and the resistivity of the particulate film.

Analysis of the oscillator feedback loop under these conditions shows that the FBAR resonant frequency will *increase* as the resistance between the FBAR terminals *decreases*. Thus, diesel exhaust particles cause an increase of the oscillator frequency at the same time as they reduce the oscillator output power. There are two ways to eliminate this problem: (1) shield the FBAR electrodes and bond wires from particles with a small drop of epoxy, or (2) use a bulk-micromachined fabrication process in which the active FBAR surface and the connecting electrodes are formed on opposite sides of a released membrane that supports the piezoelectric resonator. However, this type of anomalous

response could also be useful for detection of differences in concentration of conducting and non-conducting ultrafine aerosols and nanoparticles.

3.b. Field testing in a Berkeley dwelling: Indoor PM with episodic contributions from common PM sources

Our field test objectives included:

1) Comparing time-integrated $PM_{2.5}$ concentrations, measured with the MEMS PM monitor, to filter-based measurements, over 24- and 4-hr periods (FRM and adapted FRM, respectively),
2) Estimating the limit of detection (LOD) of the MEMS PM monitor for $PM_{2.5}$,
3) Comparing the response of the MEMS PM monitor in infiltrated ambient air, in a residence, with the responses of several real-time aerosol instruments, and
4) Identifying and prioritizing design and performance issues for further research and development on the path to commercialization.

Sampling was conducted in the same residence over two separate periods during May and June 2006. Analysis of data from the first period strongly suggested that the sensitivity of the FBAR sensor in the MEMS PM monitor had decreased substantially, compared to the results of Figs. 27 and 28. Two exposures to high concentrations of diesel exhaust may have been the cause, or the FBAR resonator may have reached the end of its useful life. For the second field-sampling period (June 2006), a second FBAR oscillator on the same chip was activated. Only data from the June field test are discussed in this report, although data from May are available upon request.

3.b.i. Description of site, instrumentation and methods

The tests were run in a 1200 square-foot two-story single-family wood-and-brick dwelling in the Berkeley hills. Fig. 30 shows a floor plan with locations of the sampling equipment. The instruments used for laboratory studies (described in Section 3.a.i) were set up in the living room, as shown in Fig 30. The house had an attic exhaust fan that could draw air from the ceiling of the test area, pulling in outdoor air through the windows and exterior doors near the test equipment.

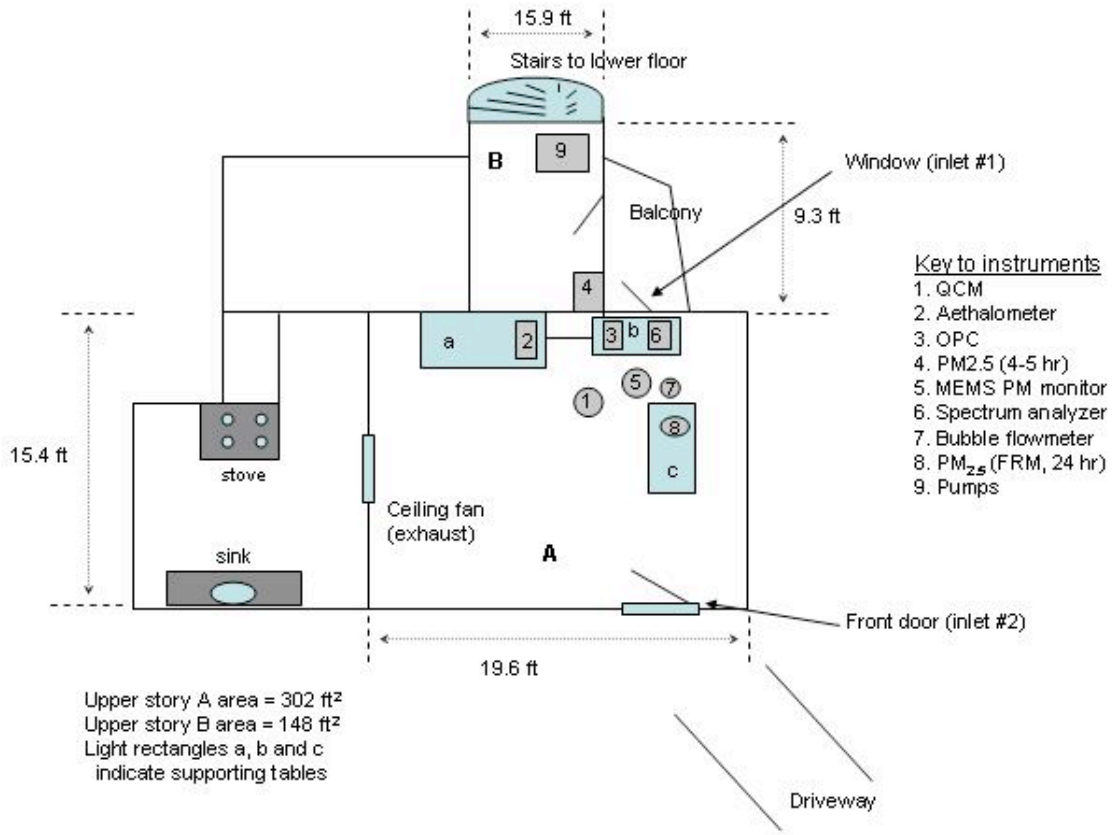

Figure 30. Floor plan of house in which field testing was conducted, showing locations of instruments, the MEMS PM monitor, and the window and door air inlets.

In addition to the instrumentation described in Section 3.a.i., the following instruments and methods were used in the field study:

Filters and pumps for determining 24-hr average $PM_{2.5}$ mass concentrations ($\mu g\ m^{-3}$) according to Federal Reference Methods. Particles larger than 2.5 μm in diameter were excluded by a Teflon-coated aluminum size selective inlet (URG, Inc.). $PM_{2.5}$ was sampled at 16.7 L min^{-1} (1 $m^3\ hr^{-1}$) onto Teflon filters (Teflo® membrane, 25 mm diameter, 3 μm pore size, Pall/Gelman, with 99.99% retention of 1 and 2 mm-diameter particles) that clamped in a stainless steel holder. The filters were equilibrated at RH 38% for 24 hrs before each weighing. A programmable pump (Gilian Aircon-2, Sensidyne) was calibrated frequently, and filters were changed every 24 hr (at midnight).

Gravimetric determination of indoor $PM_{2.5}$ mass concentrations ($\mu g\ m^{-3}$), from particles collected indoors at 100 L min^{-1} with a High Capacity Integrated Gas and Particle Sampler (Hi-C IOGAPS, URG) (Refs. 17, 18). As used in the field study, this sampling method adapted FRM methods for 4-hr, rather than 24-hr, average $PM_{2.5}$ concentrations during the periods when infiltrated ambient PM had been intentionally enriched with smoke from combustion sources nearby. The high flow rate was necessary because of the low indoor PM concentrations and the short sampling time. The IOGAPS operated with a $PM_{2.5}$ inlet (cyclone) and volumetric flow control, and particles were collected on

Teflon-coated glass fiber filters (two in series), 90 mm in diameter, equilibrated for 24 hr at 38% RH before weighing on an electronic microbalance. The filter face velocity of the Hi-C IOGAPS at 100 L min^{-1} is close to that used to collect $PM_{2.5}$ at 16.7 L min^{-1} on filters with 47 mm diameter in some versions of the Federal Reference Method for $PM_{2.5}$. The IOGAPS was operated with no denuder (gas strippers) upstream of the filters, and therefore semi-volatile organic gases were not removed from the airstream before the particles reached the filters. The modified IOGAPS sampled PM over 4-hr periods during which combustion sources were present outdoors (cigarette smoke or diesel exhaust) or indoors (cooking fumes).

Figure 31. Field test instrumentation. Top row (L to R): Quartz crystal microbalance (QCM); aethalometer; optical particle counter (OPC). Middle row: High-flow sampler for measuring episodic source-enriched $PM_{2.5}$; MEMS PM monitor; spectrum analyzer displaying FBAR resonance. Bottom row: Bubble flowmeter for use with MEMS PM monitor; FRM sampler for $PM_{2.5}$; pump and gas meter for FRM sampler.

Figure 31 shows a photographic collage of the aerosol instruments, with the MEMS PM monitor in the center and a typical FBAR resonance curve on the spectrum analyzer to center right.

3.b.ii. Monitoring protocols

Protocol 1: Responses to ambient air with windows and doors closed and no combustion sources nearby. The MEMS PM monitor operated continuously, and 24-hr average $PM_{2.5}$ concentrations were determined gravimetrically with sampling starting at midnight. The QCM, OPC and aethalometer operated throughout the field test, but data gaps exist for intervals when the instruments were malfunctioning or overloaded. Temperature and RH were monitored near the MEMS PM monitor. The FRM was used to collect 24-hr filters for $PM_{2.5}$, from midnight to midnight.

Protocol 2: Responses to ambient air with an additional combustion PM source nearby outdoors or indoors, with window or door open, and the house depressurized slightly with the attic fan operating. The FRM for $PM_{2.5}$ was adapted for 4-hr sampling while the combustion sources were operating. The FRM (24-hr gravimetric sampling for $PM_{2.5}$) continued during operation of sources. The infiltration rate of source-enriched ambient PM was adjusted based on observed changes in the PM concentrations as registered by real-time instruments, with the goal of adding sufficient PM to roughly double the recently recorded ambient $PM_{2.5}$ concentrations.

The building had an air exchange rate of approximately once per hour with the attic fan turned on, about twice the estimated rate without the fan. Ambient PM was enriched with contributions from PM generated by these sources:

- Cigarette smoke, under Protocol 2. Six cigarettes were lit and smoldered (one at a time) outside a half-open window one meter from the indoor MEMS PM monitor and the other PM monitoring instruments.

- Diesel exhaust, under Protocol 2. A diesel-powered electric generator (Red-D-Arc, Model D302L 3+12 Diesel Welder) operated for 4 hr in the bed of a pickup truck parked adjacent to the opened front door of the house. The generator electrical output powered a flood light.

- Indoor cooking under Protocol 2. Brown bread was heated in a toaster (two slices at a time) until charred in the same room as the PM monitoring equipment. (Preliminary field sampling in May 2006 at the same location showed that the ratios of UV to IR absorbance of PM from toasting bread and frying eggplant were quite similar to those of wood smoke from a neighbor's fireplace. The weather was much warmer in June, and no wood smoke was detected.)

3.b.iii. Calibration of the MEMS PM monitor: Comparison of MEMS PM monitor response to gravimetric measurements of $PM_{2.5}$ and PM_{grav}.

Comparison of the real-time MEMS PM monitor to gravimetric measurements of ambient $PM_{2.5}$ can be made by plotting the frequency difference, Δf, or the average value of df/dt for the time interval Δt as a function of the gravimetric $PM_{2.5}$ concentration for Δt. Figure 32 shows the average df/dt for durations of filter sampling Δt, using the data analysis procedures of Section 3.a.iii that account for the temperature dependence of the signal. The inset figure at the left of Fig 32 shows only the FBAR data for the 24-hr $PM_{2.5}$ measurement periods. Although these data points lie close to the origin, they appear to have the same relationship to gravimetrically determined PM as for the 4-hr $PM_{2.5}$ and the chamber results for PM_{grav} in ETS. Least squares fits to the data yield the same slope for all filter data (0.0025 kHz min^{-1} per µg m^{-3}), in agreement with chamber results (Fig. 28).

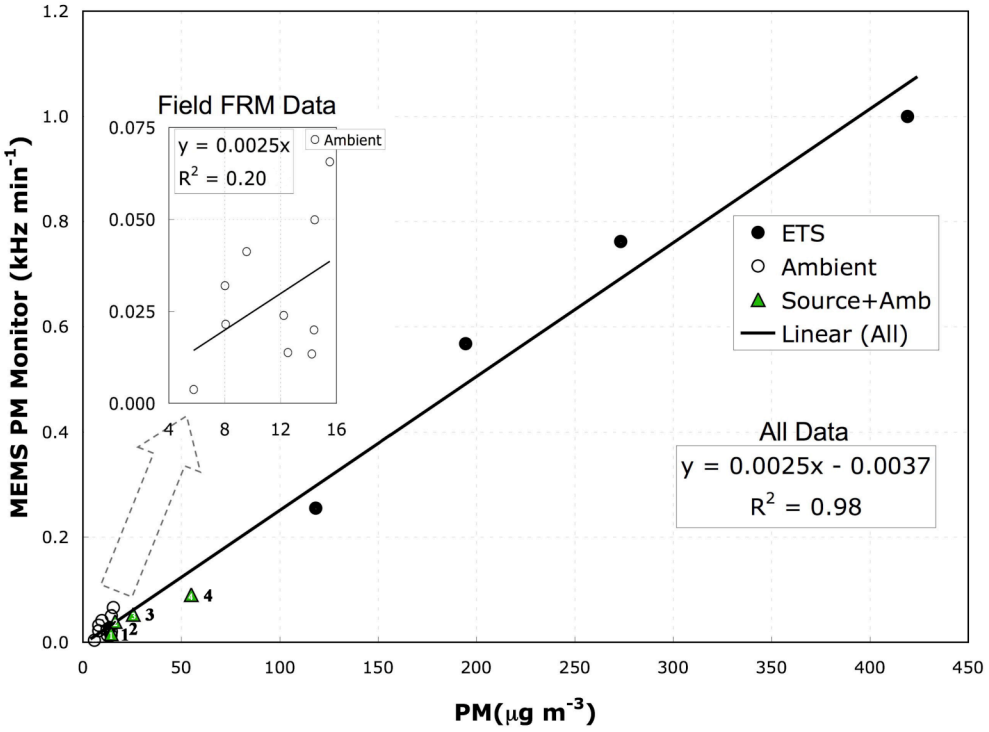

Figure 32. Calibration of the MEMS PM monitor based on environmental chamber and field tests. The FBAR signal is plotted on the y-axis as the time-weighted average derivative (kHz min^{-1}) for periods during which PM was collected for gravimetric analysis. PM concentrations are plotted on the x-axis: open circles, $PM_{2.5}$ determined with the FRM (24 hr, infiltrated ambient air); triangles, $PM_{2.5}$ determined with the adapted FRM (4 hr sampling, source-enhanced infiltrated ambient air); and filled circles, PM_{grav} (30 min to 4 hr, ETS in the environmental chamber, data of Fig. 27). The section of ambient $PM_{2.5}$ data near the origin of the plot has been expanded into the inset figure on the left. The numbers near the triangles identify the combustion sources as (1) toast, (2) diesel exhaust, (3) ETS, and (4) burnt toast. Least squares fits to the data yield the same slope for all filter data (0.0025 kHz min^{-1} per µg m^{-3}), in agreement with chamber results (Fig. 28).

3.b.iv. Influence of relative humidity on comparison of FBAR and filter data

A multivariate linear regression was conducted to assess the humidity effect on the FBAR response over 24 hour periods. Table 1 lists a compilation of chamber and field data showing measured FRM and modified FRM, average MEMS PM monitor signal, temperature, and relative humidity. These are the same PM data presented in Figure 32 but do not include the short-term gravimetric data labeled 1 - 4 in that plot. The simple bivariate regression model (MODEL A) is

$FRM_{grav} = (\alpha \times \text{Temperature adjusted FBAR signal}) + \gamma.$

The RH adjusted regression model (MODEL B) is:

$FRM_{grav} = (\alpha \times \text{Temperature adjusted FBAR signal}) + (\beta \times RH) + \gamma.$

The temperature data in the table were not used in the models because the FBAR signal was previously adjusted for temperature.

Table 1. MEMS PM Monitor response data and measured Federal Reference Method (FRM) or modified FRM

FRM_{grav}[1] ($\mu g\ m^{-3}$)	MEMS PM Monitor ($kHz\ min^{-1}$)	T (°C)	RH (%)	PM Source[2]
5.8	0.004	24.6	46.6	Ambient[2]
8.0	0.032	24.2	43.1	Ambient[2]
8.1	0.021	25.3	45.1	Ambient[2]
9.6	0.041	22.8	51.6	Ambient + Diesel[2]
12	0.024	21.1	50.1	Ambient[2]
13	0.014	28.2	32.0	Ambient + Toast[2]
14	0.027	28.1	40.0	ETS[3]
14	0.013	27.3	33.2	Ambient[2]
14	0.020	23.7	44.4	Ambient[2]
14	0.050	22.3	50.7	Ambient + ETS[2]
16	0.066	21.3	55.6	Ambient + Toast[2]
20	0.012	29.1	40	ETS[3]
120	0.255	28.6	40	ETS[3]
200	0.568	28.2	40	ETS[3]
270	0.762	27.7	40	ETS[3]
420	1.000	27.1	40	ETS[3]

[1] FRM_{grav} is either FRM or short-term gravimetric measurements using the modified FRM collection and analysis protocol described in Section 3a.i.
[2] Field data.
[3] Chamber data. RH during these sampling periods is estimated from data typical for the measurement date; RH was not measured in the chamber for the date of this experiment.

Table 2 lists the regression statistics for the two models. The results show that relative humidity plays a small, statistically insignificant (p = 0.27), role in adjusting the FBAR signal to predict 24-hr average PM concentration. The model coefficients are the inverse of those used to predict FBAR signal from FRM (e.g., 1/387 = 0.00258).

Table 2. Linear regression coefficients for models without (A), and with (B), RH included. Coefficient α, β, and γ are the response factor of the FBAR in the MEMS PM Monitor ($\mu g\ m^{-3}$ per kHz min^{-1}), the RH effect ($\mu g\ m^{-3}$ per %RH), and the intercept ($\mu g\ m^{-3}$), respectively. Statistically significant (p<0.05) coefficients are printed in bold.

MODEL	Coefficients α	β	γ	Adjusted R^2	Model p-value
A	**387**		1.7	0.985	<0.0001
B	**384**	0.699	32.5	0.985	<0.0001

3.b.v. Estimated limit of detection for FBAR-derived $PM_{2.5}$

The Hubaux-Vos detection limit procedure (Ref 19) graphically determines two sensitivity limits; a signal level, y_c, to determine, within a specified level of confidence, whether the analyte (PM) is present or not, and a detection limit, L_D that indicates the corresponding limit of detection (LOD) concentration.

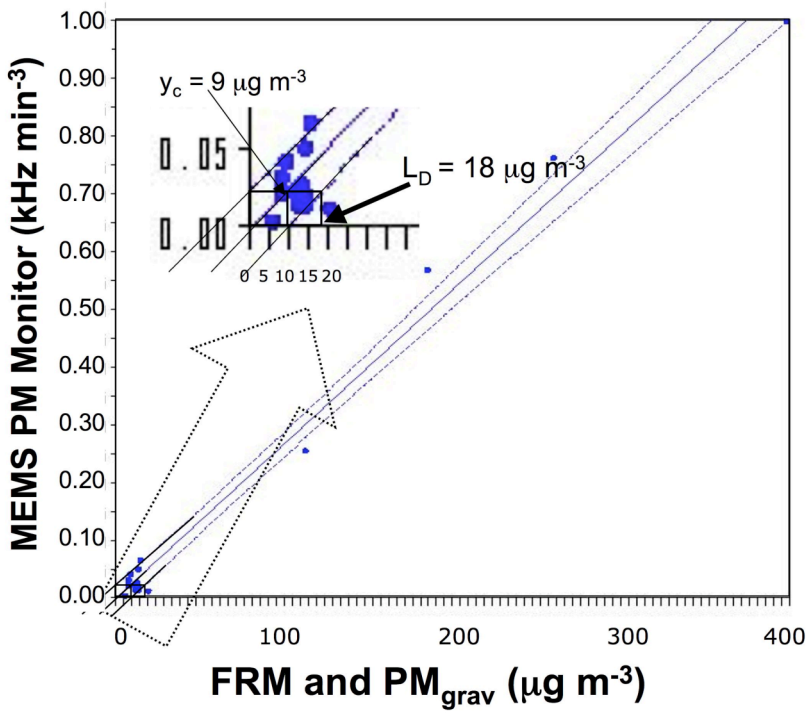

Figure 33. Limit of Detection (L_D) of MEMS PM monitor calculated using the Hubaux-Vos method is about 18 $\mu g\ m^{-3}$. The signal level y_c is approximately 9 $\mu g\ m^{-3}$. The confidence bands are calculated for a 99% confidence level.

The Hubaux-Vos method is an appropriate method for establishing the LOD of the MEMS PM Monitor as it accounts for detection across a working range of concentrations including those that are very low. This method is preferable to using only blank measurements as a basis for the LOD. The dotted lines in Figure 33 are the 99% confidence levels. The inset in Fig. 33 shows that y_c and L_D are the x-and y-intercepts of the confidence interval lines, respectively, with y_c = 9 μg m^{-3} and L_D = 18 μg m^{-3}, using the data presented in Table 1.

3.b.vi. Simultaneous monitoring of infiltrated ambient PM by MEMS PM monitor and real-time instruments

Figure 34 shows the responses of the OPC and QCM, as well as the smoothed and temperature-compensated signal from the MEMS PM monitor. The filter-based $PM_{2.5}$ concentrations are also shown, both for 24-hr and 4 hr periods when combustion sources were present outdoors (ETS, diesel exhaust) and indoors (toast). The FRM-derived 24-hr average $PM_{2.5}$ concentration was 11 ± 3 μg m^{-3}, below L_D for the MEMS PM monitor.

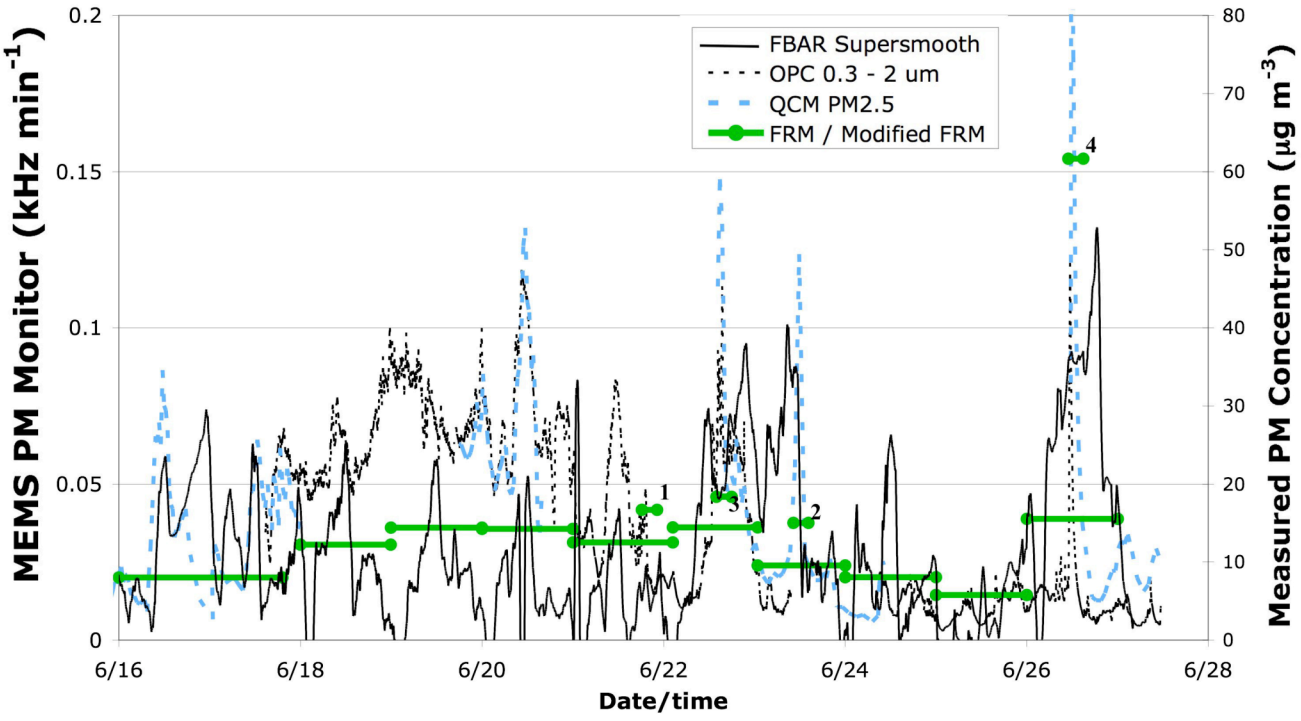

Figure 34. Responses of MEMS PM monitor (temperature-adjusted data), OPC, and QCM to infiltrated ambient air, along with 24-hr $PM_{2.5}$ concentrations. The short horizontal bars show $PM_{2.5}$ levels during periods when combustion sources operated nearby. The numbers above the short horizontal bars identify periods when the combustion sources operated as (1) burned toast, (2) diesel exhaust, (3) ETS, and (4) more toast burned. The FBAR signals were scaled with the calibration factor derived from the data shown in Fig. 32 (0.0025 kHz min^{-1} for each μg m^{-3} increase in PM concentration).

During the June field sampling period the MEMS monitor functioned well with no intervention by the investigators. However, unbroken PM records were not obtained by the QCM, OPC or aethalometer, because each of them experienced malfunctions that compromised or destroyed sections of acquired data. Fig. 34 shows that the data from the MEMS PM monitor sometimes tracked data from the QCM and OPC, and sometimes did not. The QCM and OPC usually agreed with each other, although, apart from flow rate checks, they were not calibrated right before use in the field.

Figure 35 shows the responses of the real-time instruments during the periods when cigarette smoke (June 22) and diesel exhaust (June 23) were present outdoors, near the house. In addition to signals from the QCM and OPC, available data from the UV (370 nm) and near-IR (880 nm) channels of the aethalometer are included on the plot. The relative humidity and temperature profiles are also displayed.

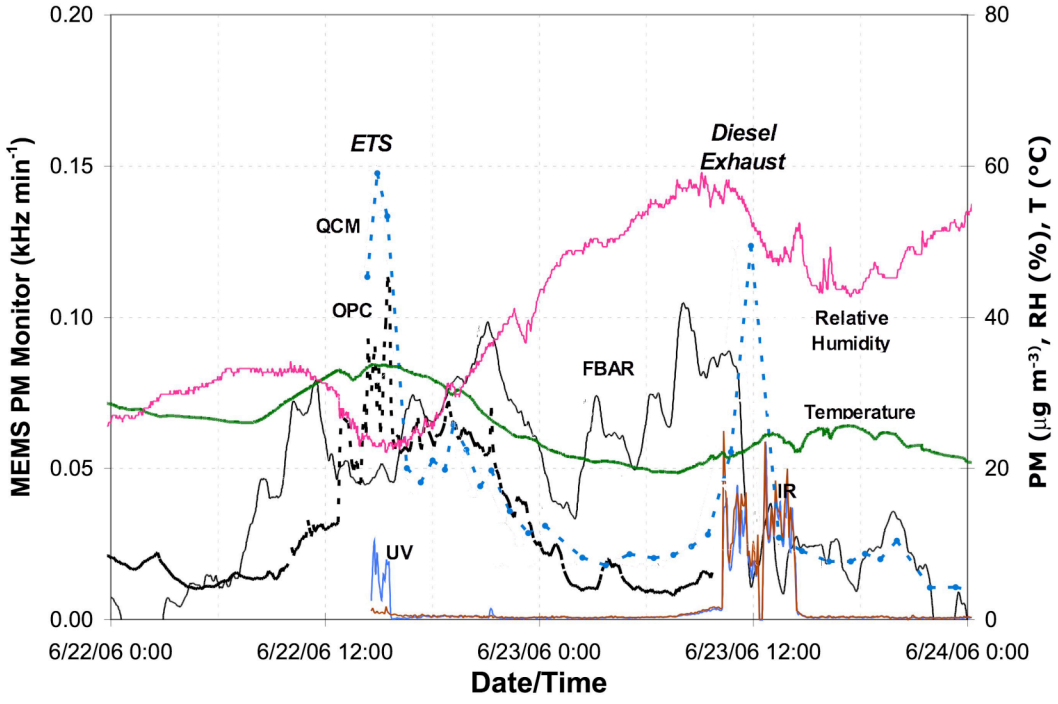

Figure 35. Responses of MEMS PM monitor, QCM, OPC and aethalometer (UV and IR in the Figure) during periods of PM generation of cigarette smoke and diesel exhaust outdoors.

Comparison of the responses of the instruments (Fig. 35) before, during and after generation of ETS and diesel exhaust in ambient air led to these observations:

1. The QCM, OPC and UV channel of the aethalometer responded to ETS more strongly than the MEMS PM monitor did.
2. The FBAR signal increased slightly in response to ETS, although its overall df/dt signal may have been more strongly influenced (negatively) by a concurrent drop in the relative humidity.
3. The aethalometer trace (from 5-min sampling periods) shows that the signal of diesel exhaust dropped in the middle of the 4-hr operating period (during a lunch break) and then rose to its previous level.
4. The QCM and both channels of the aethalometer responded to the presence of diesel exhaust.
5. The FBAR signal rose when the generator started, decreased when the generator output dropped at mid-point, and rose again when the generator output increased, to about the same level as the aethalometer signal. This part of the FBAR signal may be somewhat obscured by the aethalometer trace in Fig 35.
6. The MEMS PM monitor continued to function after its exposure to diesel exhaust (Fig 34).
7. The FBAR signal may have shown a pattern of slow response (hours) to changes in RH that obscured its response to short-term (min) response to the presence of PM sources.

The data processing procedure for the FBAR signal has already accounted for its temperature dependence, as shown in Fig. 24. The analysis presented in Table 2 showed that relative humidity did not influence the relationship between 24-hr integrated FBAR response and FRM-derived 24-hr $PM_{2.5}$ concentration. This is reasonable because of normal diurnal variation of temperature and relative humidity. However, the effect of humidity on the real-time response of the MEMS PM monitor merits further discussion. As deployed for field-testing, its components were not shielded from changes in RH (Fig. 31).

Real-time data from the field study may hold clues about the influence of RH on the performance of the MEMS PM monitor. Fig. 36 shows relative humidity, FBAR signal and filter-derived $PM_{2.5}$ concentrations for the same time period as in Fig. 34. RH varied from 17 to 65 % and averaged 44±11%, with average temperature of 24±4 C. Table 3 appears after the Figure and summarizes the distribution of maxima and minima in FBAR response among periods of increasing, decreasing and stable RH. Data are shown for the most prominent minima and maxima per 24-hr period. More than half the minima and less than half the maxima occurred while the RH rose. Most minima occurred at night and most maxima during the day. These observations are consistent with patterns of weather and expected summertime $PM_{2.5}$ generation in the Berkeley Hills.

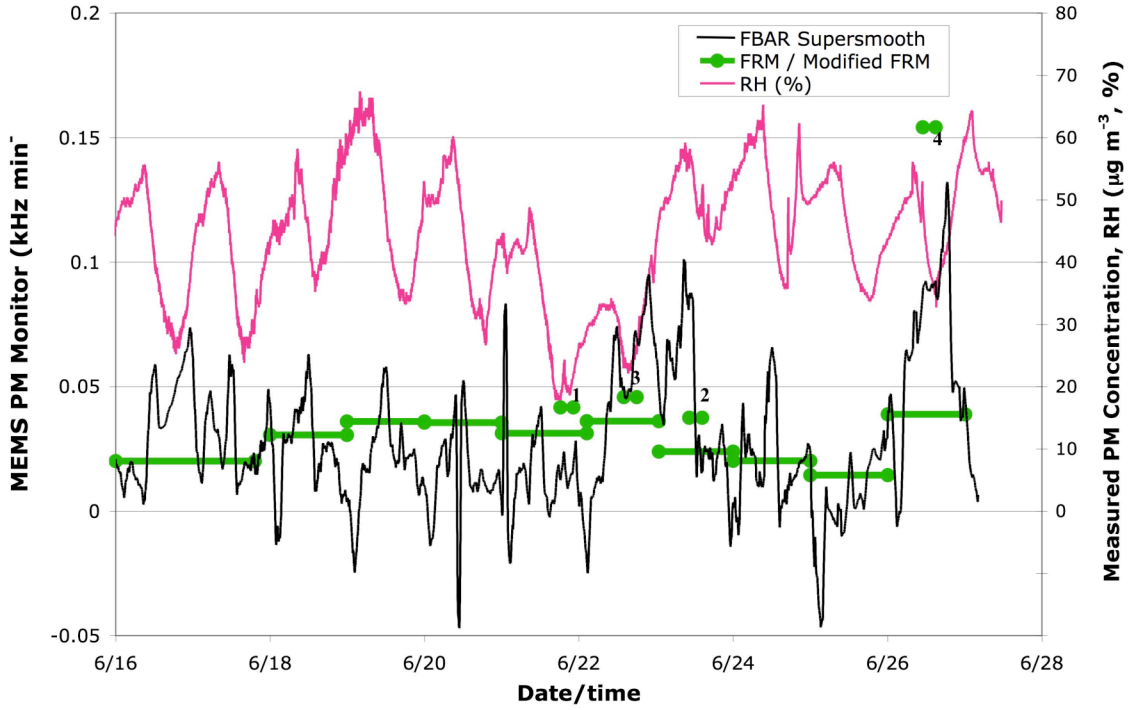

Figure 36. Relative humidity and response of MEMS PM monitor during the field study, along with 24-hr $PM_{2.5}$ concentrations and $PM_{2.5}$ levels during periods when combustion sources operated nearby. The numbers above the short horizontal bars identify periods when the combustion sources operated as (1) burned toast, (2) diesel exhaust, (3) ETS, and (4) more burnt toast. The FBAR signals were scaled with the calibration factor derived from the data shown in Fig. 32.

Table 3. Occurrence of minima and maxima in FBAR signal during periods of rising, dropping or constant relative humidity for night and day. These events occurred at average RH = 45±8% and T = 24±4 C

		#	F_{min}±sd	# RH rising	# RH dropping	# RH const
	minima	23	-0.01±0.03	12	6	5
	maxima	22	0.07±0.03	8	12	2
night		*24*	*0.03±0.05*	*19*	*0*	*5*
	minima	16	0.00±0.02	12	0	4
	negative	**9**	**-0.02±0.01**	**7**	**0**	**2**
	maxima	8	0.07±0.03	7	0	1
day		*21*	*0.04± 0.05*	*1*	*18*	*2*
	minima	7	0.00±0.04	0	6	1
	negative	1	-0.09	0	1	0
	maxima	14	0.06± 0.03	1	12	1

However, Table 3 also shows that the nine of ten periods when the df/dt signal became negative occurred at night, while the RH was increasing or remained constant (7 and 2 events, respectively). This row of the table is shown in bold. Negative values of df/dt would suggest mass loss, rather than an expected mass increase if water vapor or particle-bound water were condensing on the mass-sensing resonator. The possibility exists that

RH influenced the behavior of unprotected components of the circuitry that drove the resonator in the MEMS PM monitor during the field study.

3.b.vi. Possible design improvements for enhanced performance

The results of the pilot field testing have led to identifying and prioritizing design and performance improvements that can be addressed in further research and development on the path to commercialization:

1) Modify resonator electronics and conductor trace configuration to isolate them from sample stream in order to reduce the negative signal effects caused by ultrafine and nanoparticle diffusion deposition effects that are discussed in Section 3.a.vi.
2) Increase particle collection efficiency by increasing the temperature of the thermophoretic heater (suggested by results shown in Fig. 22).
3) Increase the fraction of particles that pass over the FBAR by narrowing the channel width. (Currently only 5% of the channel width is used for PM deposition).
4) Maintain the temperature of the MEMS PM monitor slightly above ambient to prevent water deposition
5) Modify the configuration of the optical components so that for each sensing element in the MEMS sensor array, some percentage of the PM deposits on a UV/NIR transparent window that is in the same plane as the mass sensor. The light sources would be located directly below the window. This configuration enables optical characterization by light absorption.

4. Conclusions and Recommendations

4.a. Conclusions

We have completed all the tasks listed in our proposal and later revisions of the Task and Milestone list. Considerable work is needed to improve the performance of the PM mass sensor and integrate the optical and control components before the device is ready for use as a field ready monitor that can be commercialized. The limitations of the present work at the completion of this project are listed below. However, a great amount of progress on development of this new particle measurement technology was made in this project that forms the foundation for work to come in miniaturization of PM instrumentation. We have applied for a patent and filed a record of invention for this work (Refs. 20 and 21, respectively).

We have designed, fabricated and successfully tested a compact and sensitive MEMS-based monitor for airborne particles. Tests were run in both an environmental chamber and a dwelling. The prototype monitor is characterized by a *minimum detectable added mass* of about one picogram. Based on data collected inside an occupied residence, calibrated against the $PM_{2.5}$ Federal Reference Method, the limit of detection of the device, as tested, was 18 $\mu g\ m^{-3}$. The sensor was tremendously sensitive to changes in

temperature, but simple thermal monitoring and real-time temperature correction adequately corrected for thermal drift. No significant influence from changes in relative humidity was found when comparing the MEMS PM monitor to the 24 hour FRM.

The monitor's volume, weight, and power consumption are 114 g, 250 cm^3, and no more than 100 milliwatts, respectively. A reduction of the weight and volume by factors of at least three is possible. This device also contains multiple selectable deposition and mass-sensing elements to extend the useful life of the instrument.

Since the prototype monitor incorporated a plurality (four in the present design) of mass-sensing piezoelectric resonators and small thermophoretic deposition elements, together with an optical interrogating system, the monitor can be characterized as having a long useful life (before all resonators become saturated) and speed and user convenience (samples of the deposits do not need to be sent in from the field for analysis).

Although the mass-sensing resonator operates at the relatively high frequency of 1.6 GHz, the signal can be processed so that the output can be at a much lower frequency where measurements can be made readily. The key is electrical mixing of the output of the mass-sensing resonator with that of an additional resonator that is shadowed from deposition. In this way, measurements at the much lower frequency of 5 to 10 MHz will suffice.

State of the research at the end of this project:

- The observed 24h average LOD of 18 μg m^{-3} is higher than desired for ambient and indoor $PM_{2.5}$ monitoring. The LOD and time resolution were affected by the temperature dependence and physical configuration of our prototype unit. A prioritized list of potential technical solutions for this problem has been provided above. If implemented, it is expected that the short-term (<24 hour moving average) real-time signal will be in better agreement than shown above. The prototype unit in its current form is not appropriate for making measurements at concentrations below the stated LOD. It does however meet the Federal Reference Method LOD of 30 μg m^{-3} averaged over 24 hours.
- The prototype unit has issues with conductive PM buildup. As discussed above, a reconfiguration of the sensor design to protect the resonator electronics can solve this problem.
- The optical characterization component of this project was not fully completed. Further efforts will be needed to implement this component.
- Chamber and indoor field measurements to test the device were completed but planned outdoor testing was not conducted. This will have to be completed in future work.

4.b. Commercialization Potential

Serious inquiries from several manufacturers suggest the potential commercializability of this monitor. These companies, well-known in aerosol measurement, now have non-disclosure agreements with the University of California. These potential licensees have

asked searching questions and have offered guidance and many helpful suggestions. Features that have attracted attention are convenience (small size and weight, battery operation and high sensitivity) and anticipated low cost to make (around one hundred dollars in reasonable quantities). Manufacturers have also expressed strong interest in the possibility of using just the mass-sensing module as a component that could be installed in other aerosol measuring instruments, and in wireless communications gear such as GPS receivers and in cell phones that have a position sensing capability. The marriage of these components would make feasible – both technically and economically – the widespread measurement of particles, epidemiological studies, and monitoring of power plant emissions and toxic releases, that would have substantial societal benefits.

Table 4. Comparison of characteristics of the MEMS PM monitor with those of older instruments for measuring particulates.

Type	Principle	Price	Com-plexity	Size (m^3)	Advantages	Disadvantages
MEMS PM monitor	Acoustic- wave microbalance	< $100 (est. cost to manufacture)	Low	< 0.001	Real-time mass; PM source information	
Filtration	Gravimetry; chemical and physical analysis	≥ $1K	Labor intensive	0.4	Accurate	Integrating
Aethalometer	Filtration; optical absorbance	≥ $20K	Low	0.3	Real-time	Limited PM source identification
TEOM	**T**apered **E**lement **O**scillating **M**icrobalance	≥ $20K	Low	0.4	Real-time	Non-specific
Laser Particle Counter	Light scat-tering and pulse counter	$4K – $20K	Low	0.2	Real-time	Inferred mass
Dustrac	Optical particle counter	$2K – $4K	Low	0.1	Real-time	Non-specific
QCM Impactor	Quartz crystal microbalance	≥ $20K	Labor intensive	0.3	Real-time	Complex operation

4.c. Recommendations

From the responses to our work thus far, we are encouraged to recommend design improvements based on these results, and seek follow-on funding aimed at further field testing and product design for commercialization.

Sensitivity is a major issue in selecting applications for this technology. As tested, occupational or micro-environmental peak exposures seem well suited to this sampler, but true "ambient" air often will have much less than 50 micrograms/m^3, and performance in this lower range will need to be demonstrated before the area-saturation monitoring application discussed here could provide good enough data to track typical California emission sources' plumes. That said, catastrophic events such as fires need cheap, portable monitors with real-time outputs - and the demonstrated module could easily fulfill that role once fully integrated;

Key parameters that a potential user would look at in selecting a PM monitor would include: accuracy, precision, limit of detection, particle size range, effects of particle composition. Also cost, size, weight, power, maintenance, etc.

4.d. Benefit to California

Having an inexpensive, sensitive, and easy-to-use monitor for airborne particles could lead to better understanding of the health effects of particulate exposure with their large medical costs. These monitors could become ubiquitous instruments for detecting and warning the population to avoid harmful exposure to accidental power-plant emissions, and other environmental, accidental or intentional PM releases.

5. The Future: Applications and Enhancements

Our original goal was to develop and demonstrate the ability to make a portable monitor that could measure mass concentrations of particles in a gas stream, and provide

simultaneous optical chemical characterization. We have shown that by using MEMS techniques it is possible to make a very sensitive mass sensor based on the now-ubiquitous FBAR technology. We have also shown a functioning monitor that is compact, lightweight and capable of measuring small particulate mass concentrations, as well as a proof of concept for obtaining composition information through the use of near-IR and UV LEDs and a photodiode array. A microfabricated thermophoretic heater for particulate deposition was designed, fabricated and tested successfully. Measurements also indicate that operation with battery power is feasible. Microfabrication has also permitted incorporation of a number of mass-sensing resonators in a single device, thus alleviating the need for frequent replacement or cleaning of the mass-sensing element.

Figure 35. Illustrations of possible technology and applications based on MEMS PM monitor. *Photos of aerosol monitors courtesy of TSI*

We foresee a number of applications for this type of monitor. One area is in research studies of human exposure to airborne particles: If the commercial interest already expressed in this monitor results in further development, followed by manufacture, this monitor could become an inexpensive, and therefore widely available, tool. Its applications would include measuring exposure in homes, schools, vehicles, workplaces, and in outdoor locations such as bus stops and trucking depots. We also believe that a robust, sensitive and inexpensive mass-sensing module could be added to a number of existing aerosol instruments that currently only monitor particle number.

Other long-term markets for this device may include ventilation control, aerospace, and in environmental cell biology.

By coupling these monitors to communications gear such as cell phones, GPS units and iPods, information about PM exposure could be correlated with health effects. Many organizations are already investigating the coupling of various sensors with cell phones. The five-year-old European MIMOSA project (http://www.mimosa-fp6.com/) involves many industrial and academic participants whose goal is to expand greatly the functionality of portable wireless devices such as cell phones. A local effort focusing on adding sensors to cell phones has begun in the College of Engineering at U. C. Berkeley. These possibilities are illustrated in Fig. 35.

References

1. Air Quality Criteria for Particulate Matter, EPA 600/P-99/002aF-bF. Washington, DC, U.S. Environmental Protection Agency (2004).

2. Wang, S. et al., Chemical characterization of individual airborne sub-10-micron particles and molecules, *Anal. Chem*., 78(6), 1750-1754 (2006).

3. Olin, J., and Sem, G., Piezoelectric microbalance for monitoring the mass concentration of suspended particles, *Atmos Environ.,* 5, 653-668 (1971).

4. Daley, P., and Lundgren, D., The performance of piezoelectric crystal sensors used to determine aerosol mass concentration, *Am. Ind. Hyg. Assoc. J.*, 36, 518-532 (1975).

5. Sem, G. et al., Performance of the piezoelectric microbalance respirable aerosol sensor, *Am. Ind. Hyg. Assoc. J.*, 38(11), 580-588 (1977).

6. Sem, G. and Quant, F., Automatic piezobalance respirable aerosol mass monitor for unattended real-time measurements, *Aerosols in the Mining and Industrial Work Environments*. V. Marple and B. Liu, Eds., Ann Arbor Science Pubs., Volume 3 Instrumentation, Ch. 71,.1039-1054 (1983).

7. Hinds, W., Aerosol Technology: Properties, Behavior, and Measurement of Airborne Particles, John Wiley & Sons, New York (1999).

8. McMurry, P.H et al., The relationship between mass and mobility for atmospheric particles: A new technique for measuring particle density, Aerosol Sci. Technol., 36(2), 227–238 (2002).

9. He, C., and Ahmadi, G., Particle deposition with thermophoresis in laminar and turbulent duct flows, Aerosol Sci. Technol. 29(6), 525-546 (1998).

10. Ballantine. D., White, R., et al., Acoustic Wave Sensors: Theory, Design, & Physico-Chemical Applications, Academic Press (1996).

11. Larson, J., et al., A BAW antenna duplexer for the 1900 MHz PCS band, Proc. IEEE Ultrasonics Symposium, 887–890 (1999).

12. Gundel, L. A., et al., Selective monitoring of dilute environmental tobacco smoke in ambient air with other sources, 19th Ann. Meeting American Association forAerosol Research, St. Louis, MO, (November 6-10, 2000).

13. Wagner, J., et al., Environmental tobacco smoke leakage from smoking rooms, J Occup. and Environ. Hyg., 1, 110–118 (2004).

14. Apte, M.G., Gundel, L.A., et al., Indoor measurements of environmental tobacco smoke, Final Report to the Tobacco-Related Disease Research Program, Project 6RT-0307, LBNL 49148 (2004).

15. Gundel, L.A. and Apte, M.G., Annual Reports to the Tobacco-Related Disease Research Program, Simple Exposure Indicators for Environmental Tobacco Smoke, Project 11RT-0202 (2003-2005).

16. USEPA 1997. Ambient Air Monitoring Reference and Equivalent Methods, United States Environmental Protection Agency, Federal Register 40CFR Parts 50, 53 and 58.

17. Gundel, L.A.; Lane, D.A., Sorbent-coated diffusion denuders for direct measurement of gas/particle partitioning by semi-volatile organic compounds, in Advances in Environmental, Industrial and Process Control Technologies. Gas and Particle Partition Measurements of Atmospheric Organic Compounds, Volume 2, Pages 287-332, Newark, Gordon and Breach. 1999.

18. Swartz, E., Stockburger, L., Gundel, L. Recovery of semivolatile organic compounds during sample preparation: implications for characterization of airborne particulate matter. Environmental Science and Technology 37, 597–605. 2003.

19. Hubaux, A., Vos, G., Decision and detection limits for linear calibration curves. Anal. Chem., 42(8), 849-855, (1970) .

20. Apte, MG et al. Miniaturized System for Particle Exposure Assessment. U.S. Utility Patent Application S/N 10/846,103 (2004).

21. Apte, MG et al. Miniature Monitor for Airborne Particulate Matter, Invention Disclosure, Lawrence Berkeley Laboratory, University of California, Berkeley, CA 94720. LBNL-IB2149 (2005).

List of Figures

List of Tables

Glossary

BC	Black Carbon
CMOS	Complementary Metal Oxide Semiconductor
DSP	Digital Signal Processor
ETS	Environmental Tobacco Smoke
FBAR	Film Bulk Acoustic Resonator
FRM	Federal Reference Method
GHz	Gigahertz (10^9 Hz frequency)
IR	Infrared
LOD	Limit of detection
MEMS	Micro-Electro-Mechanical System
MEMS PM monitor	Micro-Electro-Mechanical System Particulate Matter Monitor
MHz	Megahertz (10^6 Hz frequency)
OPC	Optical Particle Counter
PM	Particulate Matter
PM_{grav}	Gravimetric Determination of PM Concentration
$PM_{2.5}$	Airborne Particulate Matter less than 2.5 μm in diameter
QCM	Quartz Crystal Microbalance
RH	Relative Humidity
SSI	Size-Selective Inlet
TCF	Temperature Coefficient of Frequency
TRDRP	Tobacco Related Disease Research Program
UV	Ultraviolet